Nature of Mixed-Symmetry 2^+ States in ^{94}Mo from High-Resolution Electron and Proton Scattering and Line Shape of the First Excited $1/2^+$ State in ^{9}Be

Vom Fachbereich Physik
der Technischen Universität Darmstadt

zur Erlangung des Grades
eines Doktors der Naturwissenschaften
(Dr. rer. nat.)

genehmigte

D i s s e r t a t i o n

angefertigt von

Oleksiy Burda
aus Kharkiv (Ukraine)

Juli 2007

Darmstadt
D 17

Referent:	Professor Dr. rer. nat. Dr. h.c. mult. A. Richter
Korreferent:	Professor Dr. rer. nat. N. Pietralla
Tag der Einreichung:	17.07.2007
Tag der Prüfung:	19.11.2007

Zusammenfassung

Die vorliegende Arbeit enthält zwei Teile. Der erste beschreibt die Untersuchung von Zuständen gemischtsymmetrischer Struktur in ^{94}Mo. Der zweite beschäftigt sich mit der astrophysikalisch relevanten Linienform des ersten angeregten $1/2^+$ Zustandes in ^{9}Be.

Im ersten Teil wird die Natur der Ein- und Zweiphonon 2^+ Zustände in ^{94}Mo mit symmetrischem und gemischtsymmetrischem Charakter mit Hilfe hochauflösender inelastischer Elektronen- und Protonenstreuung in einer kombinierten Analyse untersucht. Die (e,e′)-Experimente wurden am 169°-Spektrometer des S-DALINAC durchgeführt. Daten wurden bei einer Strahlenergie $E_e = 70$ MeV und Streuwinkeln $\Theta_e = 93° - 165°$ aufgenommen. Im Energieverlustmodus wurde eine Energieauflösung von $\Delta E = 30 - 45$ keV ("full width at half maximum") erreicht. Die (p,p′)-Messungen wurden am iThemba LABS, Südafrika, an einem K600-Spektrometer bei einer Protonenenergie $E_p = 200$ MeV und Streuwinkeln $\Theta_p = 4.5° - 26°$ durchgeführt. Die typische Energieauflösung war $\Delta E \simeq 35$ keV. Die Daten wurden mit Rechnungen im Quasiteilchen-Phonon-Modell, Schalenmodell und Modell wechselwirkender Bosonen mit Proton-Neutron-Freiheitsgraden verglichen. Die kombinierte Analyse zeigt, dass die Übergänge zum ersten und dritten 2^+ Zustand eine dominante Einphonon-Struktur besitzen. Der isovektorielle Charakter des Übergangs zum gemischtsymmetrischen Einphonon-Zustand innerhalb der Valenzschale kann anhand der verschiedenen Abhängigkeit des Impulsübertrages in der Elektronen- und Protonenstreuung und der Analyse der mikroskopischen Wellenfunktionen bestätigt werden. Die Anregung der Zweiphonon-Zustände ist empfindlich auf Beimischungen von Einphonon-Komponenten. Es kann gezeigt werden, dass diese klein sind. Nach der Berücksichtigung von Zweistufen-Prozessen in der Protonenstreuung werden quantitativ konsistente Abschätzungen der Einphonon-Beiträge aus beiden experimentellen Proben erhalten.

Im zweiten Teil der Arbeit wird die Linienform des ersten angeregten $1/2^+$ Zustandes in ^{9}Be studiert. Spektren der Reaktion ^{9}Be(e,e′) wurden am S-DALINAC bei einer Elektronenenergie $E_e = 73$ MeV und Streuwinkeln von 93° und 141° mit hoher Energieauflösung bis zu Anregungsenergien $E_x = 8$ MeV gemessen. Der Formfaktor des ersten angeregten Zustandes wird aus den Daten gewonnen.

Die Impulsübertragsabhängigkeit des Formfaktors wird durch moderne "no core" Schalenmodell-Rechnungen sehr gut wiedergegeben. Die astrophysikalisch relevanten ^{9}Be(γ, n) Wirkungsquerschnitte werden aus der (e,e′)-Daten extrahiert und Resonanzparameter des ersten angeregten $1/2^+$ Zustandes in ^{9}Be im Rahmen der R-Matrix-Theorie in Einzustandsnäherung bestimmt. Gemittelt über alle verfügbare (e,e′)-Daten erhält man $E_R = 1.748(6)$ MeV und $\Gamma_R = 274(8)$ keV in guter Übereinstimmung mit dem letzten direkten (γ, n)-Experiment. Die extrahierte $B(E1)$ Übergangsstärke ist allerdings um einen Faktor zwei kleiner als in letzterem, was möglicherweise auf eine Verletzung des Siegert-Theorems am Photonenpunkt für diesen Übergang hinweist.

Summary

The present work contains two parts. The first one is devoted to the investigation of mixed-symmetry structure in ^{94}Mo and the second one to the astrophysical relevant line shape of the first excited $1/2^+$ state in ^{9}Be.

In the first part of the thesis the nature of one- and two-phonon symmetric and mixed-symmetric 2^+ states in ^{94}Mo is investigated with high-resolution inelastic electron and proton scattering experiments in a combined analysis. The (e,e$'$) experiments were carried out at the 169° magnetic spectrometer at the S-DALINAC. Data were taken at a beam energy $E_e = 70$ MeV and scattering angles $\Theta_e = 93° - 165°$. In dispersion-matching mode an energy resolution $\Delta E = 30 - 45$ keV (full width at half maximum) was achieved. The (p,p$'$) measurements were performed at iThemba LABS, South Africa, using a K600 magnetic spectrometer at a proton energy $E_p = 200$ MeV and scattering angles $\Theta_p = 4.5° - 26°$. Typical energy resolutions were $\Delta E \simeq 35$ keV. The data are compared to calculations in the quasiparticle-phonon model, shell model and interacting boson model with proton-neutron degrees of freedom. The combined analysis reveals a dominant one-phonon structure of the transitions to the first and third 2^+ states, as well as an isovector character of the transition to the one-phonon mixed-symmetric state within the valence shell by the different momentum-transfer dependence in electron and proton scattering and the analysis of the microscopic wave functions. Excitation of the two-phonon states is sensitive to admixtures of one-phonon components, which are found to be small. Quantitatively consistent estimates of the one-phonon admixtures are obtained from both experimental probes when two-step contributions to the proton scattering cross sections are taken into account.

In the second part of the thesis the line shape of the first excited $1/2^+$ state in ^{9}Be is studied. Spectra of the ^{9}Be(e,e$'$) reaction were measured at the S-DALINAC at an electron energy $E_e = 73$ MeV and scattering angles of 93° and 141° with high energy resolution up to excitation energies $E_x = 8$ MeV. The form factor of the first excited state has been extracted from the data. The momentum-transfer dependence of its form factor is well reproduced by the modern no-core shell model calculations. The astrophysical relevant $^9\mathrm{Be}(\gamma, n)$ cross sections have been extracted from the (e,e$'$) data. The resonance parameters of the first

excited $1/2^+$ state in ^{9}Be are derived in a one-level R-matrix approximation. The deduced resonance parameters averaged over all available (e,e$'$) data are E_R = 1.748(6) MeV and Γ_R = 274(8) keV in agreement with the latest direct (γ, n) experiment. However, the extracted $B(E1)$ strength is a factor of two smaller than found in the latter indicating a violation of Siegert's theorem at the photon point.

Table of contents

PART I:
Nature of the Mixed-Symmetry 2^+ States in ^{94}Mo from High-Resolution Electron and Proton Scattering

1 Mixed-symmetry states

1.1 Introduction

The low-energy spectrum of even-even nuclei is dominated by simple collective excitation modes [1]. These correlations in the nucleon motion are induced by the long-range quadrupole component of the nuclear force. In spherical nuclei with few valence nucleons, surface vibrations evolve which can be described as bosons, so-called *phonons*. In an ideal case the excitation spectrum of a vibrator nucleus is a harmonic oscillator with equidistant level spacings $\hbar w$, where phonons can couple to multiphonon states with different angular momenta and parities. For large numbers of the valence nucleons an elliptically deformed equilibrium state becomes energetically more favorable. Its vibrational modes can be divided into vibrations of the deformation parameter β (β-vibrations) and the form parameter γ (γ-vibrations).

Multiphonon excitations of atomic nuclei are interesting collective structures of the nuclear many-body system. Their existence enables us to judge the capability of the corresponding phonon modes to act as building blocks of nuclear structure. Possible deviations from harmonic phonon coupling occur due to the microscopic structure of the underlying phonon modes and serve as a sensitive source of information on the formation of collectivity in the nuclear many-body system.

The proton-neutron interaction in the nuclear valence shell has been known for a long time as the driving force for the evolution of the low-energy nuclear structure. This has been discussed in many ways, *e.g.* in terms of the evolution of collectivity in heavy nuclei as a function of the product of valence proton and neutron numbers $N_\pi N_\nu$ [2]. More recently Otsuka *et al.* have identified the proton-neutron

interaction as being responsible for the evolution of shell structure [3]. Therefore, it is interesting to study those nuclear excitations that are most sensitive to the proton-neutron interaction in the valence shell. One class of states are collective isovector valence shell excitations that are frequently called *mixed-symmetry states* (MSSs) in the terminology of the interacting boson model.

The first observation of a nuclear MSS was made in electron scattering experiments [4] on the deformed nucleus ^{156}Gd. A strong $M1$ excitation to a 1^+ state close to 3 MeV excitation energy, the scissors mode, was observed. The scissors mode has subsequently been studied mainly in electron and photon scattering experiments on deformed nuclei. Data are available for many nuclei in the rare-earth mass region and interpretations of the systematics of the centroid and the total strength as a function of deformation have been put forward [5–8].

Recently, interest has focused on the study of mixed-symmetry structures in vibrational nuclei, which are less explored. Experimentally, MSSs have been found in a number of vibrational nuclei predominantly in the mass regions $A = 90$ and 130 (see, *e.g.*, [9–16]). The best studied example is ^{94}Mo. One- and two-phonon MSSs in ^{94}Mo have been identified from large absolute $M1$ transition strengths obtained in a variety of experiments [10–13]. The present work reports a study of low-energy 2^+ states in ^{94}Mo using electron and proton scattering in a combined analysis which turns out to be a powerful tool to elucidate the multiphonon structure of nuclear excitations in vibrational nuclei.

1.2 The interacting boson model

In 1975 the interacting boson model (IBM) was introduced by Arima and Iachello [17]. The basic idea of this model is the assumption that due to the pairing force the valence nucleons outside of closed shells in the nucleus are coupled to pairs, which can be described approximately as *bosons*. In the frame of IBM the lowest collective excitations of even-even nuclei are described by these bosons in the valence space, while the contributions from nucleons in closed shells are neglected.

In the *sd*-IBM the valence space is considered to contain *s*- and *d*-bosons only. The *s*- and *d*-boson is a pair of valence nucleons coupled to total angular momentum and parity $J^\pi = 0^+$ and 2^+, respectively. It is suited for the description of many collective low-lying nuclear excitations of even spin and positive parity. The states possess a total number of bosons $N = n_s + n_d$, where $n_{s(d)}$ is the number of $s(d)$ bosons. An essential requirement to the all operators is the conservation of the total bosons number. States can be written in terms of the operators $s^\dagger$ (s boson creator), $d^\dagger_\mu$ (d boson creator with projection quantum numbers μ = -2, ..., 2), and boson annihilation operators s and d_μ. Instead of the d_μ operator $\tilde{d}_\mu = (-1)^{-\mu} d_{-\mu}$ is used as d boson annihilator. This is an essential assumption to achieve rotational invariance of the Hamilton operator.

The complete Hamiltonian of the IBM can be expanded into a sum over all n-body terms using the boson operators. Usually one restricts the Hamiltonian to include one- and two-body terms only. Also the operators can be written in terms of creation and annihilation operators, where one usually stops at the level of one-body terms. It is convenient to switch to a multipole expansion of the Hamiltonian and the transition operators. The multipole operators can then be written as

$$\begin{aligned}
\hat{n}_d &= (d^\dagger \cdot \tilde{d}) && d\text{-boson number operator,} \\
\hat{L} &= \sqrt{10}\,[d^\dagger \tilde{d}]^{(1)} && \text{angular momentum operator,} \\
\hat{Q}^\chi &= [s^\dagger \tilde{d} + d^\dagger s]^{(2)} + \chi [d^\dagger \tilde{d}]^{(2)} && \text{quadrupole operator,} \\
\hat{U} &= [d^\dagger \tilde{d}]^{(3)} && \text{octupole operator,} \\
\hat{V} &= [d^\dagger \tilde{d}]^{(4)} && \text{hexadecapole operator}
\end{aligned}$$

and the Hamiltonian takes the form

$$\hat{H} = E_0 + \varepsilon\hat{n}_d + \lambda(\hat{L}\cdot\hat{L}) + k(\hat{Q}^\chi\cdot\hat{Q}^\chi) + c_3(\hat{U}\cdot\hat{U}) + c_4(\hat{V}\cdot\hat{V}). \tag{1.1}$$

The transition operators are given by

$$\hat{T}(E0) = \gamma_0 + \beta_0\hat{n}_d, \tag{1.2}$$

$$\hat{T}(M1) = g\hat{L}, \tag{1.3}$$

$$\hat{T}(E2) = e_{eff}\hat{Q}^\chi, \tag{1.4}$$

$$\hat{T}(M3) = \beta_3\hat{U}, \tag{1.5}$$

$$\hat{T}(E4) = \beta_4\hat{V}, \tag{1.6}$$

including parity-conserving operators only as the model describes only positive parity states. For the description of negative parity states, bosons with an odd total angular momentum, *e.g.*, an f-boson ($J^\pi = 3^-$), must be added.

The simplest version of this model, the IBM-1 does not distinguish between the proton and neutron bosons. Thus, it is suited for the description of proton-neutron (pn) *fully symmetric states* (FSSs).

In contrast to IBM-1, in the IBM-2 the pn degrees of freedom is distinguished. It predicts the existence of MSSs [18] – a new class of collective nuclear states which are not fully symmetric with respect to the pn degrees of freedom. The IBM-2 introduces proton and neutron s- and d-bosons.

The Hamiltonian operator of the IBM-2 schematically has the following form

$$\hat{H} = \hat{H}_\pi + \hat{H}_\nu + \hat{V}_{\pi\nu}, \tag{1.7}$$

where $\hat{H}_\pi$ and $\hat{H}_\nu$ can be written in a multipole expansion in completely analogy to that of the IBM-1 given in Eq. (1.1). The term of the pn interaction $\hat{V}_{\pi\nu}$ contains cross terms of the proton and neutron multipole operators of the kind, *e.g.*, $(Q_\pi^{\chi_\pi}\cdot Q_\nu^{\chi_\nu})$. The transition operators are sums over the proton and neutron transition operators analog to those in Eqs. (1.2) – (1.6), *e.g.*, the $M1$ and $E2$ transition operators are given by

$$\hat{T}(M1) = \sqrt{\frac{3}{4\pi}}\left(g_\pi\hat{L}_\pi + g_\nu\hat{L}_\nu\right), \tag{1.8}$$

$$\hat{T}(E2) = e_\pi \hat{Q}_\pi^{\chi_\pi} + e_\nu \hat{Q}_\nu^{\chi_\nu}. \tag{1.9}$$

One often uses a version of the Hamiltonian of Eq. (1.7) including only the boson number operators and the quadrupole interaction, which is again motivated to the dominance of the pairing interaction. In addition, the Majorana operator

$$\hat{M}_{\pi\nu} = \left[s_\nu^\dagger d_\pi^\dagger - s_\pi^\dagger d_\nu^\dagger\right]^{(2)} \cdot \left[\tilde{s}_\nu \tilde{d}_\pi - \tilde{s}_\pi \tilde{d}_\nu\right]^{(2)} - 2\sum_{k=1}^{3} \left[d_\nu^\dagger d_\pi^\dagger\right]^{(k)} \cdot \left[\tilde{d}_\nu \tilde{d}_\pi\right]^{(k)} \tag{1.10}$$

is introduced, which represents a symmetry energy favouring states with protons and neutrons in phase. This operator causes an overall energy shift of MSSs.

1.3 F-spin

In the IBM-2 the definition of MSSs is formalized by the bosonic F-spin symmetry [19]. One finds eigenstates where wave functions are not symmetric against exchange of a proton and neutron boson. Therefore, the F-spin is introduced. F-spin is a bosonic analogon to the isospin formalism. Proton and neutron bosons have $F = 1/2$ and the z-projection is $F_z = +1/2$ for protons and $F_z = -1/2$ for neutrons. For a system of N_π proton bosons and N_ν neutron bosons the maximum F-spin is given by

$$F_{max} = \frac{N_\pi + N_\nu}{2} \geq F \geq \frac{|N_\pi - N_\nu|}{2}. \tag{1.11}$$

States with maximum F-spin, *i.e.* $F = F_{max}$ are the proton-neutron FSSs. While the MSSs have $F < F_{max}$. The investigation of such MSSs is of great interest, because they provide a better understanding of the pn degrees of freedom in heavy nuclei. In the frame of IBM-2 strong $M1$ transitions between low-lying MSSs and FSSs were predicted [18, 20].

1.4 Mixed symmetry in the Q-phonon coupling scheme

The experimental signatures of mixed-symmetry states can be clarified by the Q-phonon coupling scheme [21]. From data and nuclear models like the IBM, one learns about quadrupole collectivity in the low-lying excitations of even-even nuclei. In nearly all even-even nuclei the first excited state is a 2^+ state. Taking into account the importance of the quadrupole interaction one can build a simple and intuitive scheme describing the low-lying levels of even-even nuclei as excitations by a quadrupole operator $\hat{Q}$, hence called Q-phonon scheme. The Q-phonon scheme can be expanded to include proton and neutron Q-phonons and allows the description of mixed-symmetry states. For a symmetric coupling of the proton and neutron quadrupole operators one obtains a proton-neutron symmetric Q-phonon by

$$\hat{Q}_s = \hat{Q}_\pi + \hat{Q}_\nu. \tag{1.12}$$

The first 2^+ state, the proton-neutron fully symmetric one-phonon $2^+_{1,FSS}$ state is created by acting with the quadrupole operator on the ground state

$$|2^+_{1,FSS}\rangle = N_s \hat{Q}_s |0^+_1\rangle, \tag{1.13}$$

with a proper normalization constant N_s. A second combination of the proton and neutron quadrupole operators is

$$\hat{Q}_{ms} = a\,\hat{Q}_\pi - b\,\hat{Q}_\nu, \tag{1.14}$$

where a and b are inserted to guarantee orthogonality to the symmetric Q-phonon. Acting with this operator on the ground state leads to the mixed-symmetry one-phonon $2^+_{1,MSS}$ state,

$$|2^+_{1,MSS}\rangle = N_{ms} \hat{Q}_{ms} |0^+_1\rangle, \tag{1.15}$$

the fundamental mode or building block of the quadrupole-collective mixed-symmetry structures.

Figure 1.1 shows a Q-phonon scheme of the lowest-lying symmetric and mixed-symmetric one- and two-phonon states in even-even vibrational nuclei and their expected experimental signatures. A strongly collective $E2$ transition from the

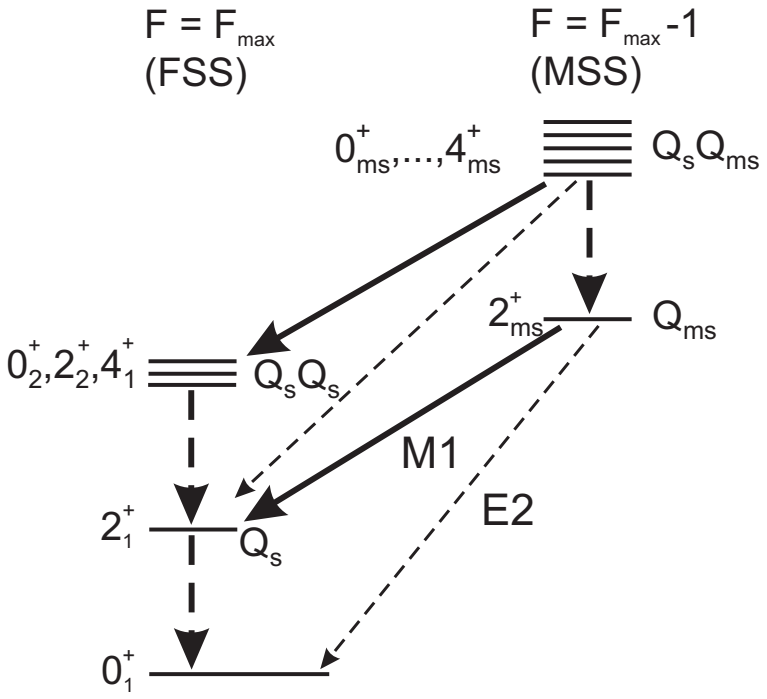

Fig. 1.1: Q-phonon scheme of low-lying vibrational one- and two-phonon symmetric and mixed-symmetry states. Dashed arrows denote $E2$ and solid arrows $M1$ transitions. Strongly collective $E2$ transitions are expected from the creation or annihilation of a Q_s-phonon. Weakly collective $E2$ transitions are expected for a Q_{ms}-phonon. Enhanced $M1$ transitions are predicted between the mixed-symmetric and symmetric states which result from the exchange of one Q_{ms}- with one Q_s-phonon.

symmetric one-phonon state to the ground state is expected, while the $2^+_{1,MSS}$ should be of comparably weak collectivity due to the destructive interference between the proton and neutron $E2$ matrix elements (see Eqs. (1.14) – (1.15)). It should be noted that in this plot the lowest 2^+ state is always the symmetric one.

Following the Q-phonon scheme, higher-lying levels are multiphonon configurations generated by coupling Q-phonons to total spin J. Two symmetric phonons form a triplet of states

$$|J^+_s\rangle \propto (\hat{Q}_s\hat{Q}_s)^{(J)}|0^+_1\rangle, \qquad \text{with } J = 0,\, 2,\, 4. \tag{1.16}$$

The mixed-symmetry Q_{ms}-phonon may couple to the symmetric Q_s as well. As

we then deal with non-identical phonons, a quintuplet of states is formed

$$|J^+_{ms}\rangle \propto (\hat{Q}_s \hat{Q}_{ms})^{(J)} |0^+_1\rangle, \qquad \text{with } J = 0,\, 1,\, 2,\, 3,\, 4. \tag{1.17}$$

In terms of IBM-2 these states have an F-spin of $F = F_{max} - 1$. It should be noted that the 1^+ member of this multiplet evolves into the well-known scissors mode for rotational nuclei discovered in ^{156}Gd [4]. Figure 1.1 summarizes the general feature, that annihilation or creation of a Q_s-phonon should lead to a strongly collective $E2$ transition, while for the Q_{ms}-phonon only a weak collective transition is expected. Within the IBM-2 approach one finds, that the exchange of a Q_{ms}- and Q_s-phonon should result in an enhanced $M1$ transition with a matrix element of the order of 1 μ_N.

1.5 Case of ^{94}Mo

The purpose of the first part of this Dissertation is an investigation of the nature of the one- and two-phonon fully symmetric and mixed-symmetry 2^+ states considering ^{94}Mo as an example. This nucleus is formed by $Z = 42$ protons and $N = 52$ neutrons. With the small number of only two valence neutrons outside the $N = 50$ neutron shell closure, this nucleus is expected to exhibit the properties of a quantum vibrator. Its low-energy spectrum is well studied and most of one- and two-phonon fully symmetric and mixed-symmetry 2^+ states have already been identified [10–13]. The relevant excitations with electron and proton inelastic scattering are studied. Since in both electron and proton scattering the one-phonon components of the nuclear wave function are predominantly excited but the isospin differs, combining both experimental probes allows to

- test the fundamental phonon character of nuclear states,
- decompose the nuclear wave function into isoscalar and isovector parts, and
- estimate the purity of the two-phonon states.

2 Experiments

2.1 Electron scattering at the S-DALINAC

2.1.1 S-DALINAC

The superconducting Darmstadt electron linear accelerator (S-DALINAC) was constructed at the Institute of Nuclear Physics of the Darmstadt Technical University [22]. It became the first superconducting continuous-wave linear accelerator of electrons in Europe. Since 1991 the S-DALINAC delivers electron beams of energies up to around 100 MeV with currents of about 10 μA routinely for a wide range of experiments on nuclear physics. A schematic layout is shown in Fig. 2.1.

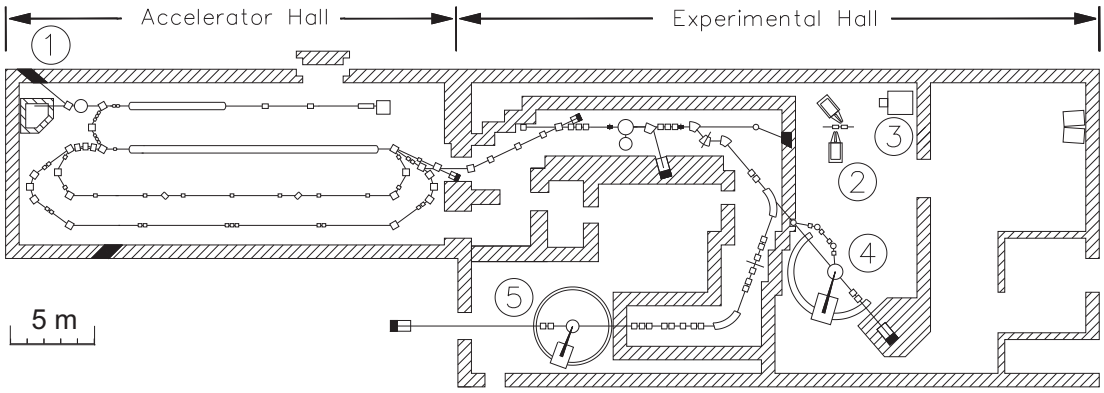

Fig. 2.1: Experimental facilities at the S-DALINAC. ① Nuclear resonance fluorescence. ② Polarizability of the nucleon. ③ $(\gamma, \gamma' \mathrm{x})$ experiments at NEPTUN tagger. ④ (e,e′x) and 180° experiments at QCLAM spectrometer. ⑤ High-resolution (e,e′) experiments at 169° spectrometer.

The electrons are emitted by a thermionic gun and then accelerated electrostatically to an energy of 250 keV. The required time structure of the electron beam for radio-frequency acceleration in a 3 GHz field is created by a chopper/prebuncher system operating at room temperature. The superconducting injector linac consists of one 2-cell, one 5-cell, and two standard 20-cell niobium cavities cooled to 2 K by liquid helium. The beam leaving the injector has an energy up to 10 MeV and can be used for nuclear resonance fluorescence ① and photoactivation experiments [23]. Alternatively, it can be bent by 180° and injected into the main

accelerator section. This superconducting linac has eight 20-cell cavities which provide an energy gain of up to 40 MeV. After passing through the main linac the electron beam may be extracted to the experimental hall or it can be recirculated and reinjected once or twice, before it is delivered to several experimental facilities. A wide range of electron scattering experiments is carried out using the QCLAM spectrometer ④ and a high-resolution electron scattering facility with a 169° spectrometer ⑤ . The QCLAM spectrometer has a large angular and momentum acceptance and is mainly used for (e,e′x) coincidence experiments [24–27] and (e,e′) at 180° scattering [28–30].

Additionally, a spectrometer for high-resolution (e,e′) experiments [31–34] which was already used with the old normal-conducting accelerator DALINAC is available. This spectrometer can be operated in a so-called energy-loss mode. The main advantage of this mode is that the resolution of the electron scattering experiment does not depend on the energy spread of the primary electron beam. In order to carry out high-resolution electron scattering experiments especially with heavy nuclei, where the level densities are high, a new detector system has recently been developed at the spectrometer [35, 36]. The old scintillator system is replaced by a modern silicon microstrip detector.

2.1.2 High-resolution electron scattering facility and 169° magnetic spectrometer

The layout of the beam transport system to the 169° spectrometer is shown in Fig. 2.2. The electron beam from the accelerator is guided to the energy-loss beam transport system. It consists of two 70° bending magnets ($E4BM01$ and $E4BM02$) symmetrically placed around an energy-defining slit system. This system includes a vertical system of slits and a horizontal comb which consists of a water-cooled copper block notched in five slits with a width of 1 mm at a distance of 2 mm. Because of the ion-optical properties of the beam-dispersion system the electron beam is dispersively broadened in horizontal direction and the electrons pass through the separate slits with different energies. The comb is needed for the beam optimisation in the energy-loss mode. Its image, that is the five strips, is projected on the detector. The beam adjustment is optimal when one spot (from elastic scattering) of minimal size is mapped on the detector. By

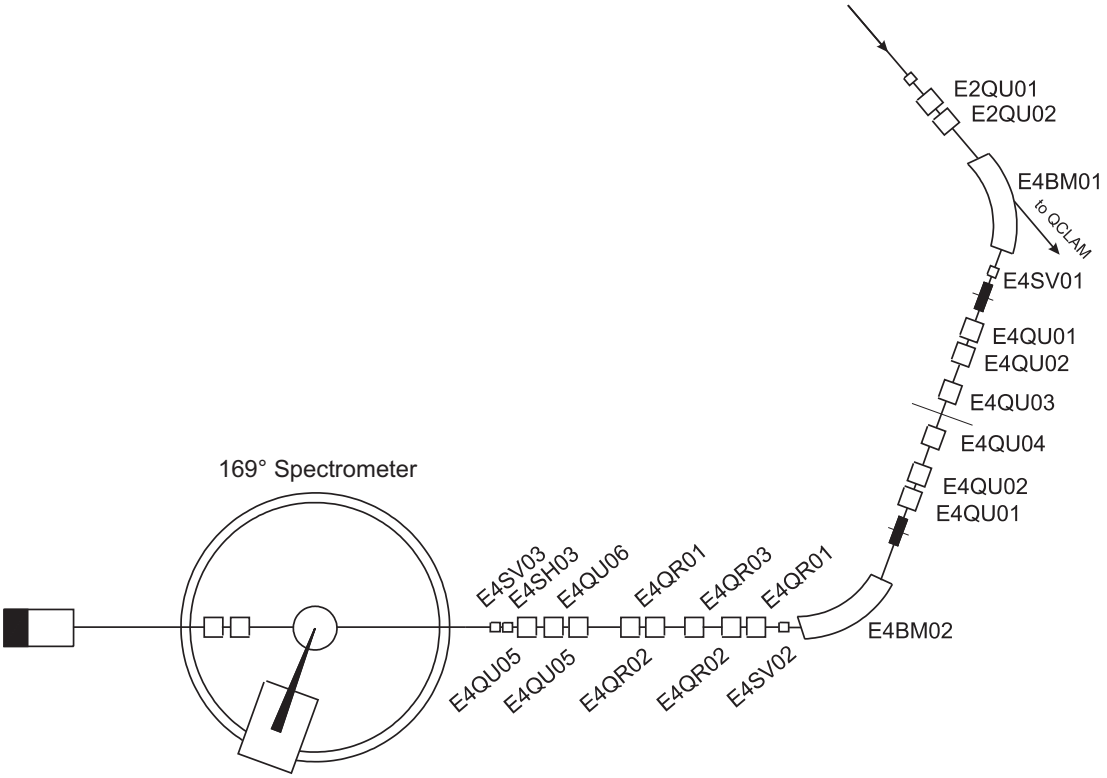

Fig. 2.2: High-resolution electron scattering facility.

different settings of the quadrupole singlets $E4QUO3$ and $E4QUO4$, the electron beam is made dispersive at the exit $E4BM02$.

Due to lack of space the spectrometer is placed vertically. A rotator, consisting of five quadrupoles (labelled as $E4QR01-05$), turns the dispersion plane to 90° in the dispersive plane of the 169° spectrometer. An accurate adjustment is achieved with the help of the quadrupole triplets $E4QU05$ and $E4QU06$. The scattering chamber allows measurements at angles of 33 – 165° in steps of 12°. A quadrupole doublet behind the target reduces the beam divergence due to multiple scattering and delivers it to a Faraday cup, which simultaneously serves as a current monitor. The scattered electrons are momentum analyzed in the 169° spectrometer.

Fig. 2.3: A photo of the 169° spectrometer. The electron beam goes from left to the right, hits the target placed in the scattering chamber ① . Electrons scattered in the solid angle Ω are momentum analysed by the dipole magnet ② and focused on the focal plane ③ where the detector system is placed.

The energy-loss spectrometer is shown in Fig. 2.3. The electron beam from the accelerator (electron beam goes from left to the right) hits the target which is placed inside the scattering chamber ① at the pivot point of the spectrometer. The scattered electrons pass the spectrometer entrance slit defining the accepted solid angle Ω, and are deflected by the dipole magnet ② to an angle of $\pi\sqrt{8}/3 = 169.7°$ (the so-called "magic" angle) which was chosen to improve the

ion-optical properties of the spectrometer [32]. At the exit of the spectrometer a vacuum chamber hosting the focal plane detector ③ is mounted.

Some important parameters of the 169° spectrometer are listed in Tab. 2.1.

Tab. 2.1: Main parameters of 169° spectrometer.

Electron energy range	$20 - 120\,\mathrm{MeV}$
Angle range	$33° - 165°$
Angle step	12°
Deflection angle	$169.7° \pm 0.1°$
Radius of central trajectory	1.0 m
Tilt of focal plane	$35° \pm 2°$
Dispersion	3.76 cm/%
Momentum acceptance	$\pm 2.1\%$
Resolution (point source, FWHM)	0.015%
Maximal solid angle acceptance	6 msr
Field strength	$0.6 - 4.0$ kG
Weight:	
Spectrometer	17 t
Shielding (safe load)	10 t

2.1.3 Focal plane detector system

The high-resolution electron scattering experiments at S-DALINAC have been successfully realized for many years using the 169° spectrometer with a focal plane detector system based on overlapping scintillators [31–34]. However, the use of plastic scintillators showed some significant drawbacks like different individual detector efficiencies which required lengthy repetitions of the measurements.

An upgrade of the complete beam line for dispersion matching including the vacuum system, the focal plane detection system and its background shielding

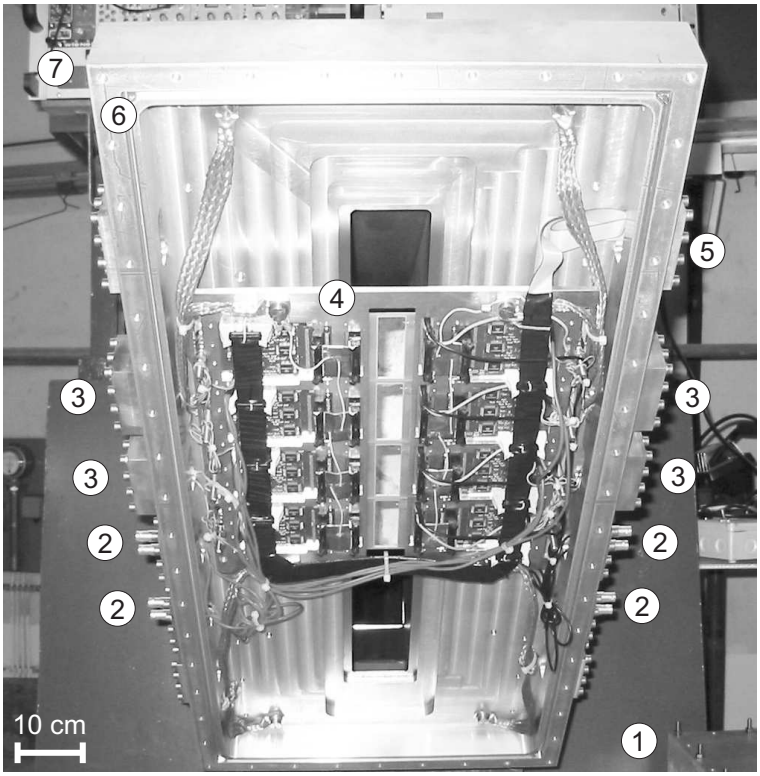

Fig. 2.4: View of silicon strip detectors mounted in the magnetic spectrometer focal plane. ① Magnetic spectrometer iron yoke. ② Vacuum connections of bias signals to the preamplifiers. ③ Vacuum connection of the preamplifiers analog signals. ④ Detector unit. ⑤ Vacuum connections of supply voltages and control signals of the preamplifiers. ⑥ Detector case. ⑦ Readout electronics and HV main adaptor (from [36]).

was recently performed. A new focal plane detector system based on modern silicon microstrip detectors together with fast readout electronics [35, 36] and a new radiation shielding [37] have been developed. The main advantages of the new detector system are the ability to process very high count rates, a high spatial resolution and an easy mechanical setup. It consists of silicon microstrip detectors and a trigger detector. Figure 2.4 presents a picture of the Si microstrip detector. There is no single-strip detector available covering the full focal plane length of 24 cm. Therefore, four single-strip detectors were mounted together, each providing 96 strips with a thickness of 500 μm and a pitch of 650 μm. The guard ring around the 96 strips and the printed circuit board carrier result in an inactive zone of about 7 mm (or 10.5 strips) between two adjacent detectors. In

the measurements these blind spots in the spectrum are shifted in regular time intervals by slight variations of the spectrometer magnetic field.

For background suppression a trigger detector system is used. It consists of a 40 cm long plastic scintillator with a thickness of 5 mm (material NE102A) and 40 cm long Cherenkov counter of 5 cm thickness run in coincidence.

2.2 Proton scattering at the iThemba LABS

2.2.1 Separated-sector cyclotron facility

The inelastic proton scattering experiments were carried out at the iThemba LABS (Themba means hope, and LABS stands for Laboratory for Accelerator Based Sciences) located in Somerset West, near Cape Town, South Africa.

Figure 2.5 shows schematically the layout of the main accelerator together with related installations for various experiments and applications. A primary beam of protons and light ions can be produced and pre-accelerated by an injector cyclotron SPC1. Another injector cyclotron SPC2 with an external ion sources is used for polarized protons and heavy ions. The heart of the facility is a separated-sector cyclotron (SSC), a four-sector machine with a sector angle of 34°. After the injection into the cyclotron the particles start to gain energy while circulating in the RF and magnetic fields on the cyclotron orbits, the largest proton energy gain per turn being about 1 MeV. The maximum energy achievable for protons is 200 MeV. At the exit high-energy beams of various ions can be extracted and used in a wide range of applications, like radioactive isotope production, proton and neutron therapy of cancer patients and fundamental nuclear physics research.

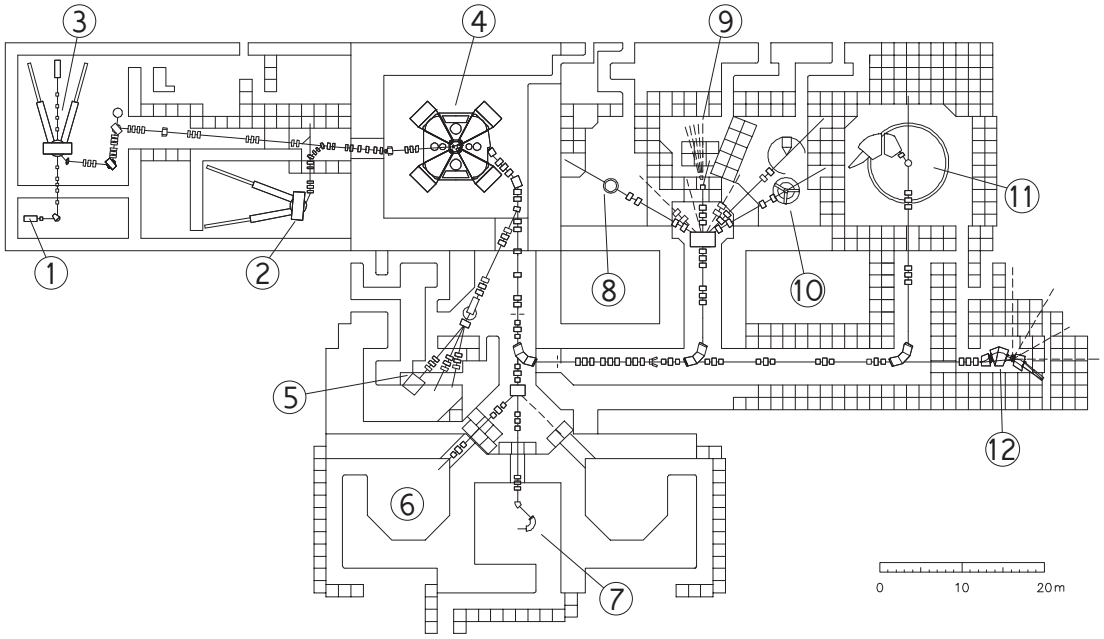

Fig. 2.5: A layout of the experimental facilities at the iThemba LABS. ① ECR ion source. ② SPC1 injector cyclotron. ③ SPC2 injector cyclotron. ④ Separated-sector cyclotron. ⑤ Radioactive isotope production. ⑥ Proton therapy. ⑦ Neutron therapy. ⑧ Experiments with charged particles. ⑨ Experiments with neutron beams. ⑩ γ-spectroscopy. ⑪ K600 magnetic spectrometer. ⑫ Beam swinger magnet.

2.2.2 K600 spectrometer

For the present experiment proton beams were delivered to the experimental hall of the K600 spectrometer, which has been used intensively for high-resolution inelastic scattering experiments [38–41]. A layout of the experimental setup is displayed in Fig. 2.6. The beam enters the scattering chamber ① with a set of

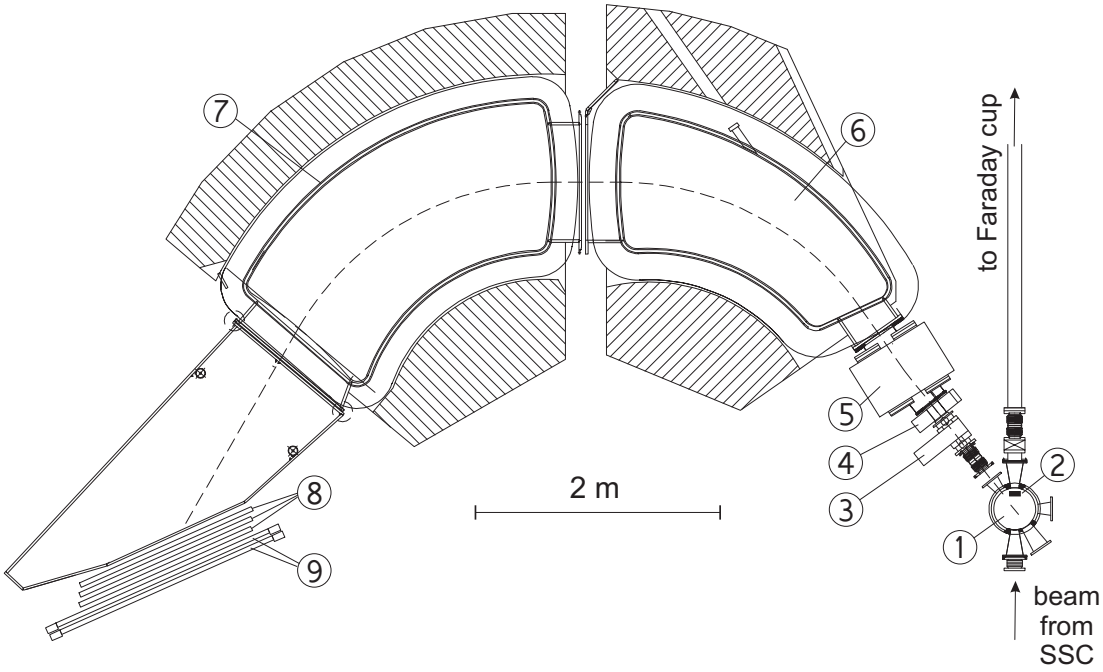

Fig. 2.6: An overview of the K600 spectrometer at the iThemba LABS. ① Scattering chamber. ② Internal Faraday cup for small-angle scattering experiments. ③ Set of collimators. ④ Sextupole magnet. ⑤ Quadrupole magnet. ⑥ First dipole. ⑦ Second dipole. ⑧ Two horizontal and one vertical drift chamber. ⑨ Two plastic scintillators.

targets put on a target ladder. For measurements under small scattering angles an internal Faraday cup ② is used as a beam dump. Scattered protons on the target are collimated by one of the collimators installed on the carousel ③ , which defines the solid angle. The protons then pass through the ion-optical system of the K600 spectrometer, which consists of a sextupole magnet ④ , a quadrupole magnet ⑤ for vertical focussing, and two horizontally bending dipole magnets ⑥ and ⑦ . The particles are focused on the focal plane of the spectrometer, where a detector system is placed, consisting of three miltiwire drift chambers ⑧ ,

two horizontal and one vertical for event reconstruction. Two plastic scintillators ⑨ located behind the drift chambers serve as a trigger and particle identification detector.

2.3 Lateral dispersion matching technique

For the experiments discussed in this thesis, high energy resolution is of utmost importance in order to resolve the nuclear transitions of specific interest. Usually, the energy resolution is limited by the relative beam energy spread (typically $\Delta E/E \simeq 10^{-3}$). This limitation can be overcome if the characteristics of the beam are matched to those required by the ion-optical properties of the spectrometer by adjusting the beam line parameters.

The lateral dispersion matching technique is realized in both experimental facilities at the S-DALINAC and at iThemba LABS, respectively. The basic principle of lateral dispersion matching (often also called *energy-loss mode*) is shown schematically in Fig. 2.7 and requires an adjustment of the beam dispersion, emittance and spot size at the target position using beam line focussing and steering elements to match with the ion-optical properties of the spectrometer. In the conventional *dispersive mode* (on the l.h.s. of Fig. 2.7), the beam is focussed to a spot at the target. If the scattered particles are not monoenergetic, but have some energy spread ΔE, then trajectories having slightly different energies will cross it under slightly different angles. The image resolution in such a case will be affected by the initial energy spread of the beam. In the *lateral dispersion matching mode* (on the r.h.s. of Fig. 2.7) the beam is projected on the target by the beam transport system as an extended spot. Its size corresponds to the beam energy spread ΔE. Thus, one adjusts the dispersion of the beam at the target position in such a way that the trajectories of different momenta (energies) traverse different path lengths through the magnetic field of the spectrometer, and are focussed back on the focal plane at one spot (solid line), thus providing better image resolution almost unaffected by the residual spread of the primary beam energy. If the particles lose some energy δE by passing through the target the beam spot on the focal plane is displaced (dashed line) by the distance determined

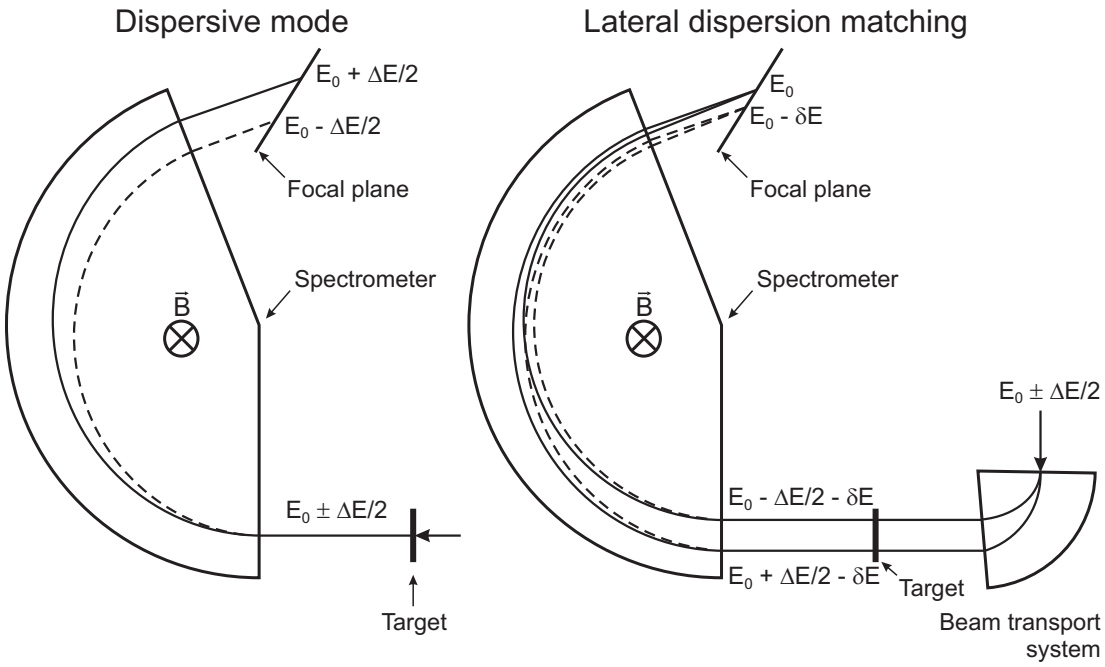

Fig. 2.7: Dispersion matching technique. Left: dispersive mode. The position and the angle of scattered particles at the focal plane depend on the initial energy spread ΔE, which thereby limits the resolution. Right: lateral dispersion matching. It allows to improve the resolution by spatially spreading the beam spot at the target position according to the dispersion of the beam, matching it to that of the spectrometer.

by the energy loss of electrons in the target. That makes the system sensitive to the energy loss in the target only and independent of the energy spread of the beam. Such a technique allows to achieve a relative energy resolution down to $\Delta E/E \simeq 1{\times}10^{-4}$.

2.4 Experiments

The (e,e′) experiments were carried out at the high-resolution 169° magnetic spectrometer of the S-DALINAC. The data presented on the l.h.s. of Fig. 2.8 were taken at an incident electron beam energy $E_e = 70$ MeV and scattering angles Θ_e = 93° – 165° with typical beam currents of 2 μA. For the measurements a self-supporting ^{94}Mo target enriched to 91.6% with an areal density of 9.65 mg/cm^2

was used. In dispersion-matching mode an energy resolution $\Delta E \simeq 30 - 45$ keV (full width at half maximum, FWHM) was achieved.

High-resolution (p,p′) measurements were performed at the cyclotron of iThemba LABS, South Africa, using the K600 magnetic spectrometer. The target consisted of a self-supporting molybdenum foil enriched to 93.9% ^{94}Mo of 1.2 mg/cm^2 areal density. Data were taken at a proton energy $E_p = 200$ MeV and scattering angles $\Theta_p = 4.5^\circ - 26^\circ$ with currents varying from 1 to 30 nA, depending on scattering angle. On the r.h.s. of Fig. 2.8 examples of the spectra measured at scattering angles of 6°, 9°, 22°, and 26° are presented up to an excitation energy of 4 MeV. Typical energy resolutions were $\Delta E \simeq 35$ keV (FWHM).

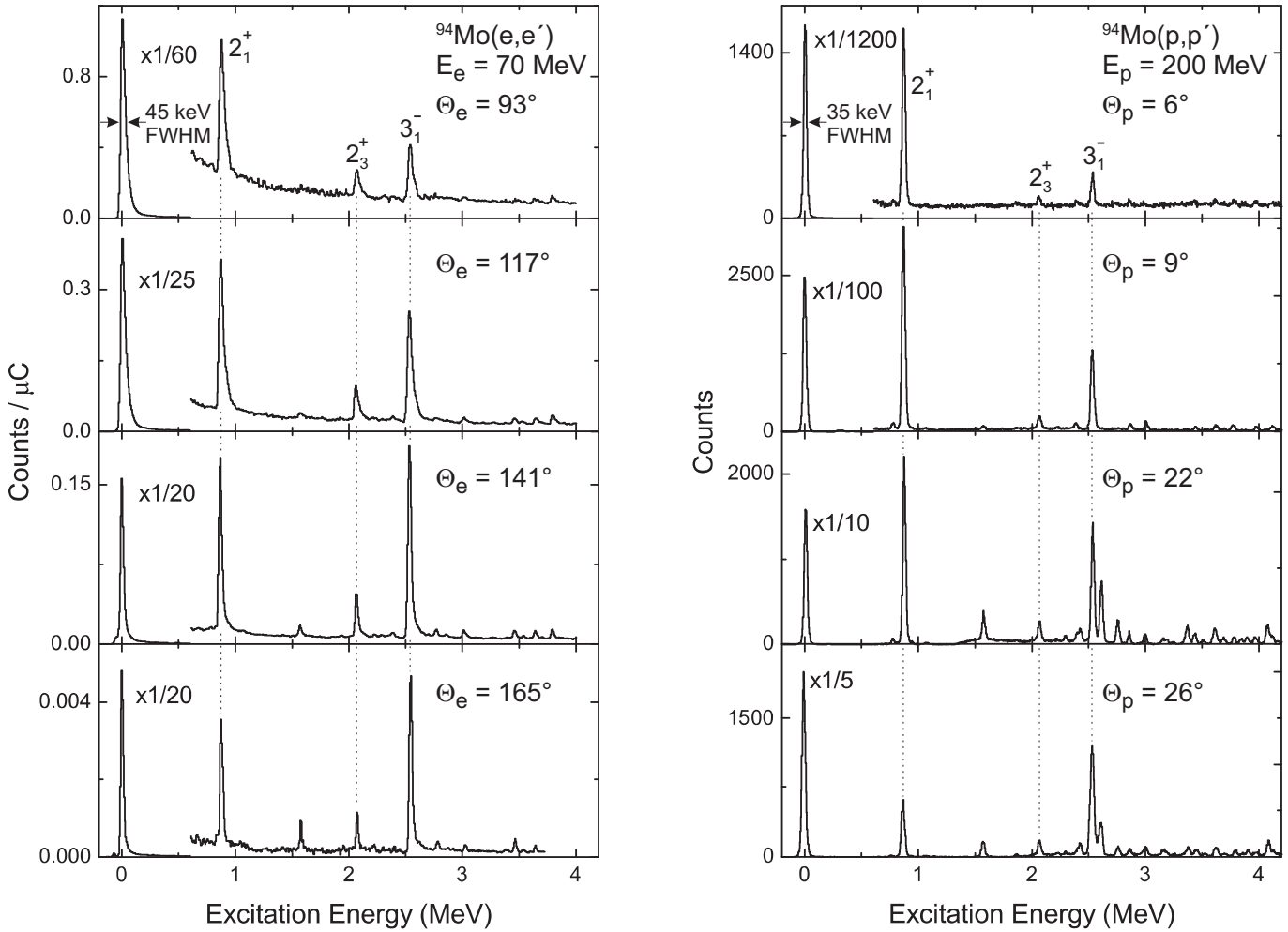

Fig. 2.8: Representative spectra of ^{94}Mo(e,e′) reaction (left) and ^{94}Mo(p,p′) reaction (right) measured in the present work.

The prominent peaks correspond to the elastic line, the collective one-phonon FSS (2_1^+, $E_x = 0.871$ MeV) and 3_1^- ($E_x = 2.534$ MeV) states, and the suggested one-phonon 2^+ MSS (2_3^+, $E_x = 2.067$ MeV). The dominance of the transitions to the 2_1^+ and 2_3^+ states indicates already the concentration of one-phonon strength in their wave functions, as visible in Fig. 2.9.

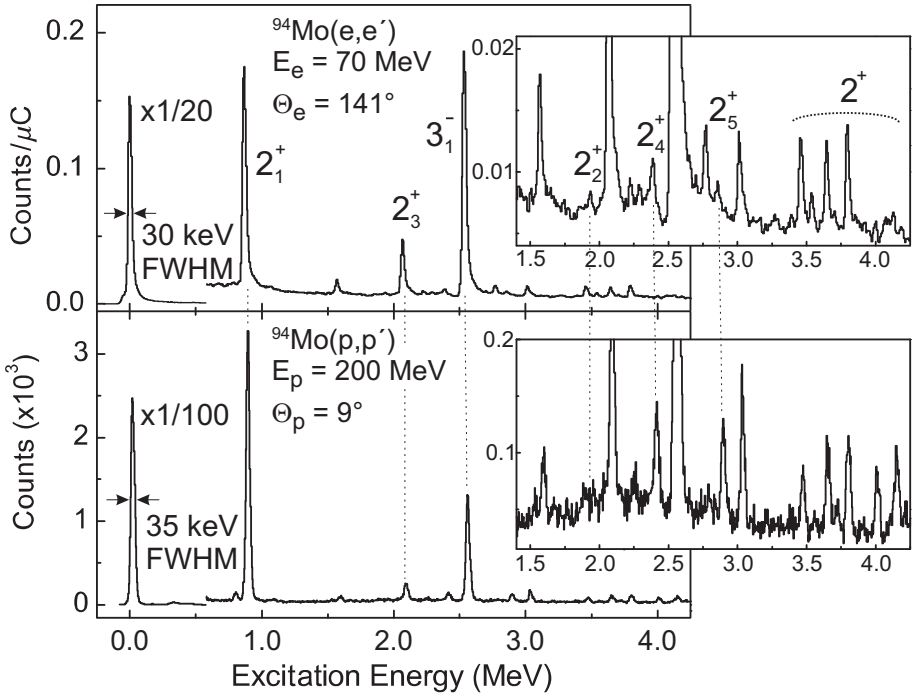

Fig. 2.9: Top: spectrum of the ^{94}Mo(e,e′) reaction at $E_e = 70$ MeV and $\Theta_e = 141°$. Bottom: spectrum of the ^{94}Mo(p,p′) reaction at $E_p = 200$ MeV and $\Theta_p = 9°$. Insets: zoom on the $E_x = 1.5$ – 4 MeV region of the respective spectra.

The candidates for the two-phonon FSS (2_2^+, $E_x = 1.864$ MeV) and MSS (2_5^+, $E_x = 2.870$ MeV) are only weakly excited, but the extended view (insets of Fig. 2.9) demonstrates their observation as well as that of all other 2^+ states known [13] up to 4 MeV due to the good energy resolution in both experiments.

3 Data analysis

3.1 Electron scattering

3.1.1 Decomposition of the spectra

The spectra of the present ^{94}Mo(e,e′) experiment are assumed to have no instrumental, but physical background due to radiative processes. For the analysis of the discrete states the line area content A_{in}^{exp} was determined by adjusting a model function for the line shape of the measured spectrum using the program FIT [42]. For the description of electron scattering an asymmetric Gaussian function is used as a line shape with a width modified on the low-energy side due to energy losses of the electron in target. The radiative tail is approximated by a hyperbolic function continuously connected to the Gaussian function. For the decomposition of the spectra the following parameterisation [43] of the line shape was used

$$y = y_0 \cdot \begin{cases} \exp\left[-\ln 2 \cdot (x - x_0)^2 / \Delta x_1^2\right] & x \leq x_0 \\ \exp\left[-\ln 2 \cdot (x - x_0)^2 / \Delta x_2^2\right] & x_0 < x \leq x_0 + \eta \Delta x_2 \\ A/(B + x - x_0)^\gamma & x > x_0 + \eta \Delta x_2, \end{cases} \tag{3.1}$$

with

x_0 the energy at the peak,

y_0 the count rate at the peak maximum,

$\Delta x_{1,2}$ the half widths at half maximum for $E_x < x_0$ and $E_x > x_0$, respectively,

η the starting point of the radiative tail in units of Δx_2,

γ the exponent of the hyperbolic function of the radiative tail.

The parameters A and B result from the condition of a continuously differentiable connection of the individual functions at the intersection point $x_0 + \eta \Delta x_2$.

The area content A_{in}^{exp} is calculated as an integral of the function used in the parameterisation. Because the spectra of the inelastic scattered electrons cannot be

measured up to infinitely small energies, the area under the peak is integrated up to a cutoff limit $E_{cutoff} = x_0 + 5\Delta x_1$. The calculated peak area A_{in}^{exp} is multiplied by correction factors for the radiation effects

$$A_{in} = A_{in}^{exp}\, e^{\delta_S+\delta_B+\delta_I}. \tag{3.2}$$

The first of the radiative corrections, the Schwinger correction δ_S, accounts for the loss of the peak area due to those electrons degraded because of the emission of real soft photons as well as emission and absorption of virtual photons of any energy. The bremsstrahlung correction δ_B takes into account effects which cause an asymmetric distortion of the peak due to small angle scattering from electrons and nuclei other than the scattering nucleus. The third effect, Landau straggling (ionization correction) δ_I, describes the broadening of the peak due to energy loss from atomic excitations and ionisation. A detailed description of these corrections can be found, *e.g.*, in [44].

3.1.2 Energy calibration

The momentum acceptance of the spectrometer is about 4%. That means, for example, an energy byte is only 2.92 MeV for an incident electron energy E_e = 73 MeV. To measure larger energy regions one needs to perform measurements for different settings of the spectrometer magnetic field. Then it is necessary to perform also a calibration measurement for each spectrometer magnetic field setting using known prominent transitions. The calibration is performed using a direct correspondence between the scattered electron energy E' and a channel number N. One has to take into account the mean electron energy loss ΔE in the target. This can be roughly estimated with the help of the following expression

$$\Delta E\,[\mathrm{MeV}] = 1.4 \times t_{eff}\,[\mathrm{g/cm^2}], \tag{3.3}$$

where t_{eff} is the effective target thickness. For measurements at the scattering angles $\Theta_e \leq 141^\circ$ the target is placed in transmission geometry (perpendicular to the scattering angle bisector). In this case the electrons have an effective path length $t_{eff} = t/\cos(\Theta_e/2)$, where t and Θ_e are the target thickness and the scattering angle, respectively. Measurements at angles $\Theta_e > 141^\circ$ are possible only in the reflection geometry, the target is placed parallel to the scattering

angle bisector. In this case the effective path length of the electrons in the target is $t_{eff} = t/\sin(\Theta_e/2)$.

The energy of scattered electrons taking into account the target nucleus recoil and the electron energy before and after scattering can be expressed as

$$E' = \frac{(E_e - 0.5\,\Delta E) - E_x(1 + \frac{E_x}{2Mc^2})}{1 + \frac{2\,(E_e - 0.5\,\Delta E)}{Mc^2}\sin^2(\Theta_e/2)} - 0.5\,\Delta E = f(N), \tag{3.4}$$

with E_i, E_x, M being the initial electron energy, excitation energy and mass of the target nucleus, respectively.

Due to the fact that the spectrometer magnetic field is quite homogeneous, the function $f(N)$ is expected to be linear. Thus, solving Eq. (3.4) one gets a quadratic equation relative to E_x. This calibration is valid only for a given spectrometer magnetic field setting and has to be performed independently for other settings. In order to combine the excitation energy spectra measured at different magnetic field settings it is necessary to reduce all spectra to the same energy bin size.

To calibrate the ^{94}Mo(e,e$'$) spectra the precisely known excitation energies (from Ref. [13]) of the prominent transitions in ^{94}Mo to states like 0^+_1, 2^+_1, 2^+_3, 3^-_1 were used.

3.1.3 Determination of the cross sections

The absolute value of the differential cross sections can be calculated from the peak area A^{exp}_{in} corrected for the radiative correction (see Eq. (3.2)), for the detection efficiency (discussed later in Sec. 8.2), and for the dead time of the electronics according to

$$\frac{d\sigma}{d\Omega} = A^{exp}_{in} \cdot \frac{1}{\Delta\Omega} \cdot \frac{e}{It} \cdot \frac{M}{t_{eff}\,N_A}, \tag{3.5}$$

where $\Delta\Omega$ is the spectrometer solid angle [sr], It the accumulated charge [C], M the mass number [g/mol], t_{eff} the effective areal density of the target [g/cm^2] and N_A the Avogadro number [1/mol].

3.1.4 Error estimate

The measured (e,e′) cross sections contain not only statistical but also the following systematic errors which contribute to the total uncertainty in the determination of the cross sections:

- inaccuracy in the determination of the solid angle ($\approx 5\%$),
- uncertainty in the determination of the accumulated charge in the Faraday cup ($\approx 5\%$),
- error in the dead-time correction ($< 1\%$),
- target inhomogeneity ($\approx 5\%$).

The errors although being systematic ones were treated as independent of each other and therefore added quadratically resulting in a total systematic error of about 9%. The statistical uncertainties are taken from the error in the area definition during the fit of the lines in the spectrum with model functions.

3.2 Proton scattering

3.2.1 Peak deconvolution and background subtraction

The total number of events of each state was obtained from a deconvolution of the spectrum by a peak fitting software [45]. The physical background in the spectra from the hydrogen contamination in the target was estimated by an empirical smooth function.

3.2.2 Energy calibration

In binary reaction measurements, the energy of the scattered particle E' is given by the following equation

$$E' = E_i - (E_x + \Delta E + E_{rec} + Q), \tag{3.6}$$

where E_i, E_x, ΔE, E_{rec}, and Q are the energy of incident particle, excitation energy of the target nucleus, energy loss of incident particle when penetrating the target, the recoil energy and the reaction Q-value, respectively. For scattering reactions $Q = 0$. In order to calibrate the ^{94}Mo(p,p$'$) spectra the accurately known excitation energies (Ref. [13]) of the prominent transitions to the 0_1^+, 2_1^+, 2_3^+, 3_1^- levels in ^{94}Mo were used.

3.2.3 Determination of the cross sections

Cross sections were calculated similar as described in Sec. 3.1.3. The line areas A_{in}^{exp} were corrected for the detection efficiency of the multiwire drift chambers (the total efficiency is about 85%), and for the dead time of the electronics.

3.2.4 Error estimate

The measured (p,p$'$) cross sections contain not only statistical but also the following systematic errors which contribute to the total uncertainty in the determination of the cross sections:

- inaccuracy in the determination of the solid angle ($\approx 5\%$),
- uncertainty in the determination of the accumulated charge in the Faraday cup ($\approx 5\%$),
- error in the dead-time correction ($\approx 5\%$),
- target inhomogeneity ($\approx 5\%$).

The systematic error was estimated to be 10%. The statistical uncertainties are taken from the error in the area definition during the fit of the lines in the spectrum with model functions. The total error was calculated to be the square root of the sum of the squared systematic and statistical errors.

4 Results and discussion

4.1 Details of the model calculations

To extract quantitative information on the phonon character of the observed states, the momentum-transfer dependence of the cross section has been calculated using microscopic shell model (SM), quasiparticle-phonon model (QPM) and IBM-2 wave functions.

4.1.1 Shell model

The shell model Hamiltonian is taken as

$$H = H_0 + V_{res}, \tag{4.1}$$

where the term H_0 is the mean field part of the nuclear Hamiltonian which describes independent motion of non-interacting particles in a self-generated average potential. The term V_{res} is the residual interaction. It causes a superposition of particle-hole configurations in the wave function of excited states and thus (amongst others) the appearance of collective states in nuclear spectra.

It is not possible to take into account the full Hilbert space of the Hamiltonian of Eq. (4.1) for practical model calculations, due to the large (infinite) number of particles and orbitals. For the two-body interaction 2^A terms play a role, producing a matrix that is impossible to diagonalize. Subsequently, the shell model employs the idea of a truncation of the Hilbert space by the concept of an inert core. In this concept a nucleus with magic proton and neutron numbers is regarded as closed, *i.e.* orbitals below the magic number do not contribute. In addition, the number of orbitals above the inert core is limited to only a few orbitals. This limitation is in principle arbitrary – the model space is chosen in order to describe certain physical properties of the atomic nucleus. In this way the number of orbitals and the number of valence particles outside the closed shells are limited. The problem is reformulated in terms of an effective Hamiltonian and effective operators, so that the Schrödinger equation is modified

$$H\psi = E\psi \longrightarrow H_{eff}\psi_{eff} = E\psi_{eff}, \tag{4.2}$$

where the derived wave functions ψ_{eff} contain generally only a small part of the real and complicated wave functions ψ due to the truncation. Nevertheless, the success of the shell model shows that this small part often carries the main physical properties.

Defining a core, the Hamiltonian can be written in the second quantization form as

$$H = \sum_{k}^{n_{val}} \epsilon_k \, a^{\dagger}_{\rho_k} \, a_{\rho_k} + \\ + \sum_{\rho_a,\rho_b,\rho_c,\rho_d,J,M,T} \langle \, (\rho_a \rho_b)_{JT} \, | \, V_{12} \, | \, (\rho_c \rho_d)_{JT} \, \rangle \, (a^{\dagger}_{\rho_a} \, a^{\dagger}_{\rho_b})^{T}_{JM} \, (a_{\rho_c} \, a_{\rho_d})^{T}_{JM}. \tag{4.3}$$

where n_{val} is the number of single-particle states in the adopted valence shells, ϵ_i are single-particle energies which are taken from data and incorporate the mean-field potential representing the binding energies of a particle on the i-th orbital, $a^{\dagger}_{\rho}$ creates and a_{ρ} annihilates a particle on the single orbital $|\rho\rangle = |n, l, j, m_j, t = 1/2, t_z\rangle$ and T is the isospin of the coupled particles.

Shell-model calculations for the present case described in [46] are based on the low-momentum nucleon-nucleon (NN) interaction V_{low-k}. The basic idea is that the interaction needs only to be defined up to a resolution scale which allows to resolve the physics one is interested in. Using the renormalization group, one starts from one of the high-precision NN interactions and integrates out the high-momentum components above a cutoff Λ [47]. It should be chosen such that the NN scattering phase shifts and deuteron properties are exactly conserved at low momentum. It has been shown that as Λ is lowered to 2.1 fm^{-1}, which corresponds to a distance scale at $1/\Lambda \sim 0.5$ fm, the V_{low-k} interaction is universal and independent of the specific parameterization of the NN interaction [48,49]. Since the V_{low-k} interaction is energy independent it is suitable for SM calculations in any nuclear region [50]. In these SM calculations a V_{low-k} interaction derived from the CD-Bonn [51] potential with a cutoff $\Lambda = 2.1$ fm^{-1} was used.

Shell-model calculations in this work were carried out with the shell model code OXBASH [52] using the effective interaction described above to reproduce mixed-symmetry structure in ^{94}Mo. As in previous shell-model work using the simplified surface delta interaction [53], ^{88}Sr was chosen as the inert core and the proton-neutron model space was taken to be: $\pi\,(2p_{1/2}, 1g_{9/2})$ and

$\nu\,(2d_{5/2}, 3s_{1/2}, 1g_{7/2}, 2d_{3/2}, 1h_{11/2})$. The single-particle energies were taken from the experimental values in ^{89}Sr and ^{89}Y.

Due to the truncation of the single-particle basis the collectivity of low-lying states is underestimated. To reproduce the $B(E2)$ transition strengths to the one-phonon FSS and supposed one-phonon MSS effective quadrupole charges, $e_p = 1.98\,e$ and $e_n = 1.38\,e$ have been used determined by a fit to the experimental values.

4.1.2 Quasiparticle-phonon model

In this model $1p1h$ excitations are projected on a space of one-phonon states, whose properties (excitation energies and internal fermion structure) are obtained from solving quasiparticle-RPA equations [54]. When the phonon basis is built, the wave function of excited states are written as a combination of interacting one- and multiphonon configurations (see, *e.g.*, [55]). Multiphonon configurations are obtained by coupling of one-phonon configurations. In general, the size of the space of all multiphonon configurations is the same as in the no-core SM if a similar single-particle basis is used. Thus, in realistic calculations the QPM also requires a basis truncation. It is performed following two main principles. First of all, very complex N-phonon configurations are cut out. In practice, the most complex configurations included in the wave function of low-lying states are of 3-phonon nature. Secondly, only configurations with an energy below some maximum value are accounted for. In fact, these truncation principles are physically motivated. The density of complex configurations is rather low below the particle threshold and the influence of truncated configurations at high excitation energies on the properties of low-lying states is very weak. Altogether it allows to consider the QPM calculations as rather realistic from the point of view of the basis completeness at low excitation energies.

Although in scattering reactions the levels are mainly excited via one-phonon components of the wave function, multiphonon configurations are also very important because they are responsible for fragmentation of the one-phonon strength. The structure of excited states in the QPM calculations is obtained from a diagonalization of the QPM Hamiltonian for the above-mentioned wave functions. The diagonalization yields eigenenergies of excited states and their wave functions in

terms of phonons or $1p1h$, $2p2h$, and $3p3h$ configurations. The model Hamiltonian

$$H = H_0 + H_{pair} + V_{res} \tag{4.4}$$

contains an average field H_0, monopole pairing interaction H_{pair} for protons and neutrons, and a residual interaction V_{res} written in a separable form. A Woods-Saxon potential with a standard set of parameters is used as mean field. The monopole pairing strength is fixed from description of pairing energies [56]. The strength of the residual interaction is adjusted to reproduce the properties (excitation energy and transition strength) of the 2_1^+ and 3_1^- levels.

In the calculations reported below, multiphonon configurations have been built from phonons with $J^\pi = 1^\pm - 6^\pm$. They have been truncated at 7 MeV. The calculations are similar to the ones in Ref. [57,58] except for the treatment of the particle-particle channel of the residual interaction which is not included here. Additionally, results (referred to as pure QPM) will be presented in which excited states are described as pure one- or two-phonon states with the same phonons as in the full calculation but with the interaction between them being artificially switched off.

Contrary to the SM, the single-particle basis in QPM calculations is rather complete and includes all mean-field levels from $1s_{1/2}$ to quasi-bound levels in the continuum. For this reason, no effective charges are needed to describe collectivity of low-lying excited states.

4.1.3 Interacting Boson Model – 2

The IBM-2 description of (e,e′) form factors followed the approach suggested in [59]. The radial dependence of the transition densities was obtained in a generalized-seniority shell-model calculation [60, 61] using the V_{low-k} interaction as input. This calculation is done separately for neutron and proton bosons. The basic transition densities of $1p1h$ transitions are summed with coefficients determined from a calculation of transition rates within the IBM-2. In a two-level approximation the transition densities of the one-phonon FSS and MSS states can be obtained as

$$\begin{aligned} \rho_{FSS}(r) &= A_1\,\rho_\pi(r) + B_1\,\rho_\nu(r), \\ \rho_{MSS}(r) &= A_2\,\rho_\pi(r) + B_2\,\rho_\nu(r). \end{aligned} \tag{4.5}$$

Using the vibrational U(5) limit coefficients A_1, B_1 and A_2, B_2 are given by [62]

$$
\begin{aligned}
A_1 &= \sqrt{\frac{5}{N_\pi + N_\nu}}\, N_\pi\, e_\pi\, \frac{1}{\sqrt{B(E2)_\pi}}, \\
B_1 &= \sqrt{\frac{5}{N_\pi + N_\nu}}\, N_\nu\, e_\nu\, \frac{1}{\sqrt{B(E2)_\nu}}, \\
A_2 &= \sqrt{\frac{5\, N_\pi\, N_\nu}{N_\pi + N_\nu}}\, e_\pi\, \frac{1}{\sqrt{B(E2)_\pi}}, \\
B_2 &= -\sqrt{\frac{5\, N_\pi\, N_\nu}{N_\pi + N_\nu}}\, e_\nu\, \frac{1}{\sqrt{B(E2)_\nu}},
\end{aligned}
\tag{4.6}
$$

where $N_{\pi(\nu)}$ describes the number of proton (neutron) bosons and $B(E2)_{\pi(\nu)}$ the reduced transition strengths obtained from the charge transition proton (neutron) densities $\rho_{\pi(\nu)}$, respectively. The experimental effective proton and neutron boson charges $e_\pi = 10.7\,\mathrm{e\,fm^2}$ and $e_\nu = 2.3\,\mathrm{e\,fm^2}$ were taken from [13].

For the quantitative discussion below this approximation should show little difference to a calculation with a realistic IBM parameters. Fit of the IBM-2 model parameters to the data on ^{94}Mo leads to value between U(5) (vibrator) and O(6) (γ-soft rotor) dynamical limits. However, little difference for analytic predictions of U(5) and O(6) for the data are of interest.

4.1.4 Cross section calculations

The electron scattering cross sections were calculated in the Distorted Wave Born Approximation (DWBA) using the code of Ref. [63]. The radial transition charge densities calculated by the theoretical models described above have been used as input. The theoretical proton scattering cross sections were calculated using the code DWBA05 [64] with the RPA amplitudes obtained in the QPM and the one-body transition densities obtained in the SM to describe the excited states. The t-matrix parametrization of Franey and Love [65] at 200 MeV was used as effective projectile-target interaction.

4.2 Shell model and quasiparticle-phonon model predictions

In Fig. 4.1 a comparison of the experimentally known [13] excitation energies of the lowest 2^+ states in ^{94}Mo with the QPM and SM predictions is shown. The QPM calculation reproduces the number of experimentally known 2^+ states in the energy interval up to 4 MeV studied indicating a sufficiently large model space and also predicts their excitation energies with an accuracy of better than 300 keV allowing to establish a one-to-one correspondence between calculated states and the data. The SM results show a little bit worse energy correspondence but reproduce the mixed-symmetry structure in ^{94}Mo.

4.3 One-phonon fully symmetric and mixed-symmetry states

Figure 4.2 presents the cross sections of the transitions populating the one-phonon FSS and MSS in ^{94}Mo as a function of momentum transfer q. The dominance of these transitions observed in Fig. 2.9 already indicates the concentration of the one-phonon strength in their wave functions. It should be noted that the (e,e′) data exhibit a very similar q-dependence, while it differs for the (p,p′) data for both states. Since proton scattering is a predominantly isoscalar nuclear probe, the relative shift of the maxima and minima in the cross sections points to an isovector character of the 2^+_3 state.

It should be noted that all theoretical results shown hereafter are absolute without a further normalization to the data. The SM results provide a good description of the (e,e′) form factors and the (p,p′) cross sections except at higher momentum transfers, where correlations outside the valence space become important. The IBM-2 form factors are very similar to the SM results. Considering an overall uncertainty of about 25% due to the choice of the effective interaction [66], the QPM accounts well for the proton scattering results but shows a systematic shift of the form factor maximum compared the electron scattering data. Related dis-

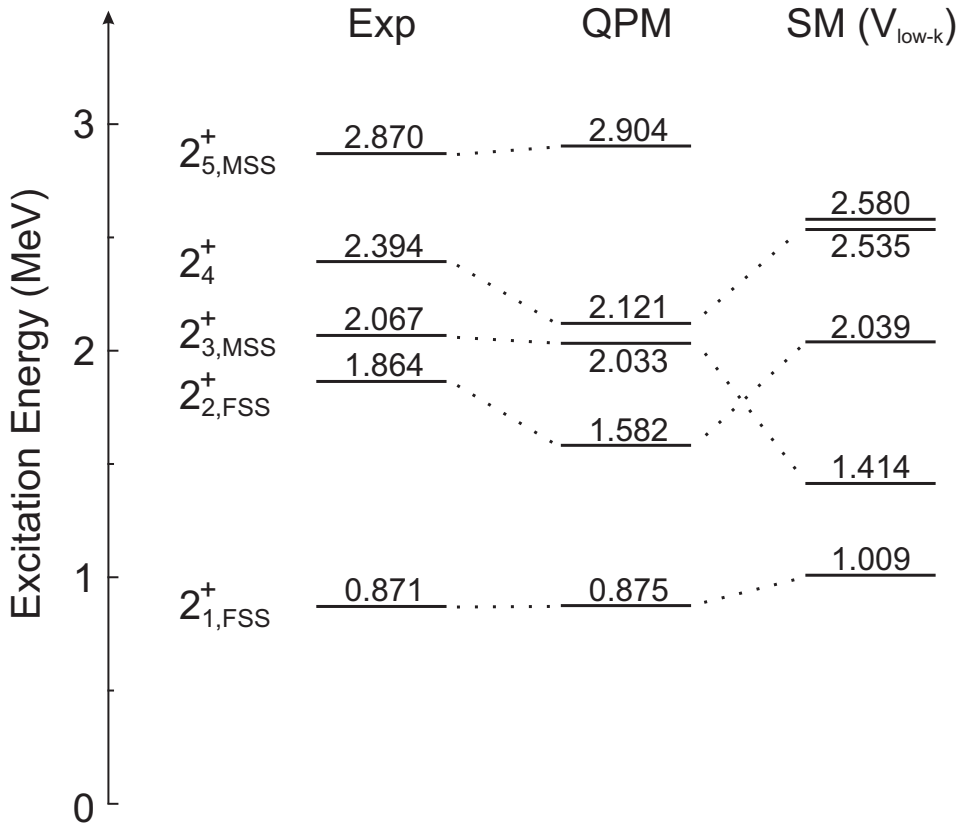

Fig. 4.1: Experimental and theoretical excitation energies predicted by the QPM and SM (V_{low-k}) for the lowest 2^+ states in ^{94}Mo. The one- and two-phonon FSS are labelled as $2^+_{1,\mathrm{FSS}}$ and $2^+_{2,\mathrm{FSS}}$. The one- and two-phonon MSS are labelled as $2^+_{3,\mathrm{MSS}}$ and $2^+_{5,\mathrm{MSS}}$, respectively. The correspondence between experimental and theoretical excitation energies is indicated by dotted lines.

cussions are given in the next section. Overall, all models agree on the one-phonon character of the 2^+_1 FSS and 2^+_3 MSS.

4.4 Isospin character of the one-phonon states

Due to different sensitivity of the one-phonon states to proton and neutron degrees of freedom, the combined information from electron and proton scattering results permits an extraction of their F-spin character. Based on successful description by microscopic model results one can analyze the structure of the one-phonon

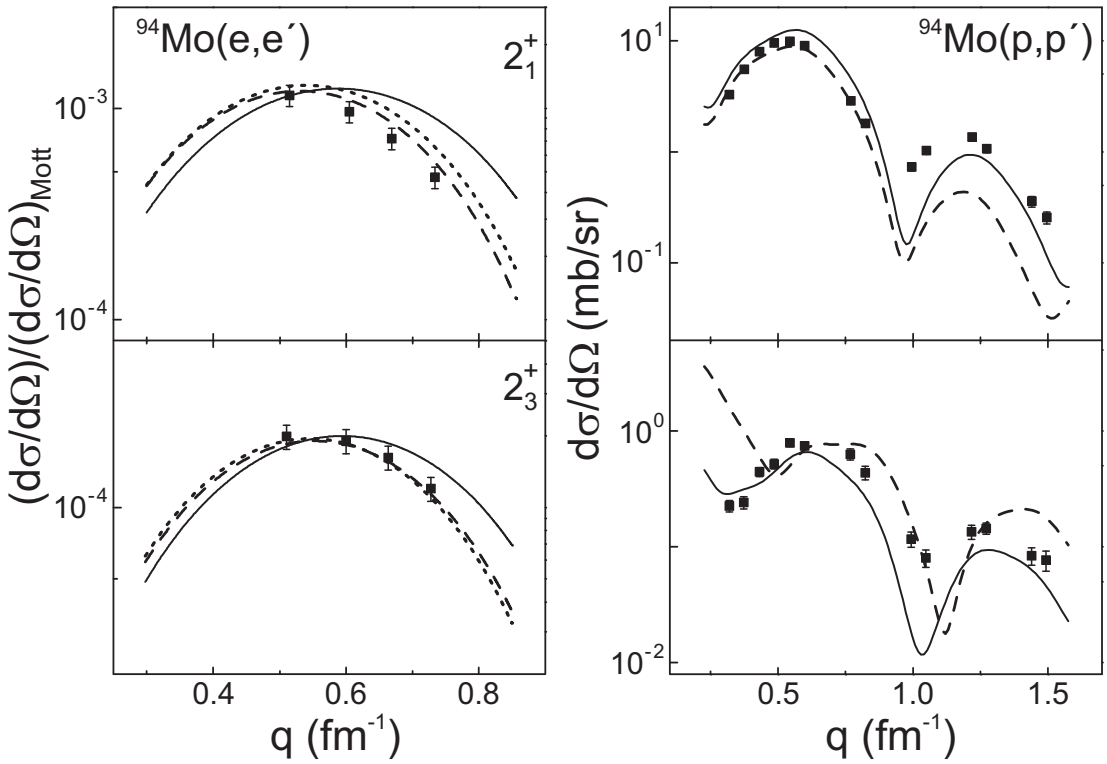

Fig. 4.2: Momentum-transfer dependence of the one-phonon FSS (top) and MSS (bottom) excitation cross sections in ^{94}Mo. Left: electron scattering. Right: proton scattering. The data (full squares) are compared to QPM (solid lines), SM (dashed lines), and IBM-2 (dotted lines) predictions described in the text.

states in terms of their main particle-hole configurations. In Tab. 4.1 the main proton and neutron components of the QPM and SM wave functions of the one-phonon FSS and MSS are presented. Note, that the SM results are given in terms of one-body transition densities.

Tab. 4.1: Main configurations of the QPM and SM wave functions.

Main configuration	$2^+_{1,FSS}$		$2^+_{3,MSS}$	
	QPM	SM (V_{low-k})	QPM	SM (V_{low-k})
$\pi\,(1g_{9/2}\,1g_{9/2})$	0.60	0.39	0.64	0.51
$\nu\,(2d_{5/2}\,2d_{5/2})$	0.70	0.55	-0.71	-0.33

The QPM and SM predict the dominant proton and neutron terms in the wave function of the FSS to have the same, and that of the MSS opposite signs. That confirms the picture of dominantly isoscalar character of the FSS and isovector character of the MSS in the valence shell.

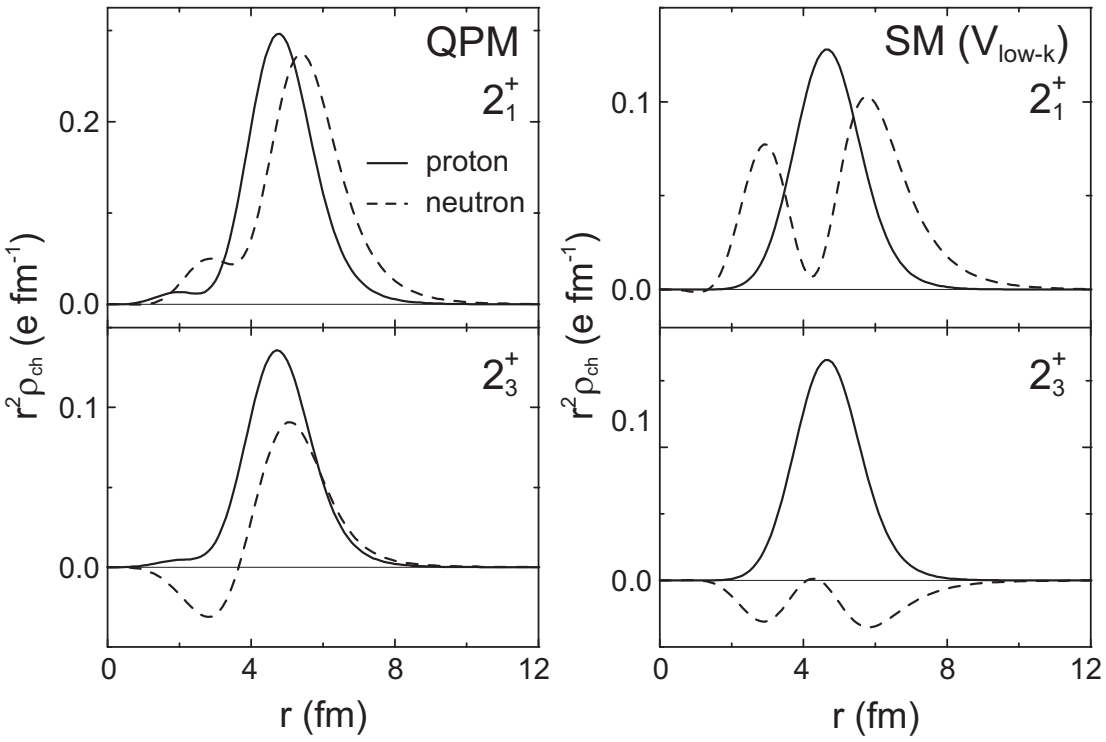

Fig. 4.3: Radial transition proton (solid line) and neutron (dashed line) charge densities for the one-phonon FSS (top) and MSS (bottom). Left: QPM predictions. Right: SM (V_{low-k}) predictions.

Figure. 4.3 presents the radial charge transition densities of protons (solid lines) and neutrons (dashed lines) predicted by the QPM (left) and SM (right) for the transition populating one-phonon FSS (top) and MSS (bottom). While for the one-phonon FSS in the nuclear interior protons and neutrons oscillate in phase representing the predominantly isoscalar nature, the behavior of the QPM and SM transition charge densities for the suggested one-phonon MSS is different: in the nuclear interior the protons and neutrons move out of phase in accordance with the isovector nature of the 2_3^+ state in the valence shell.

The transition densities of the both states are peaked at the nuclear surface and thus provide evidence of the collectivity of these states. Looking at the scale of

the ordinate, the QPM predicts these states to be more collective than the SM.

While the number of protons (neutrons) changes from 40 to 50 the $1g_{9/2}$ subshell is filled in. In ^{94}Mo this subshell is fully occupied for neutrons and contains two protons only. In the (e,e′) calculations for the QPM only protons contribute, in the SM both protons and neutrons are taken into account. As a result the maximum of (e,e′) form factors predicted by the QPM is displaced to larger momentum transfers that is seen in Fig. 4.1 of the section above. The experimental charge radius in the proton mean-field description by a global Woods-Saxon potential within the QPM is underestimated. An artificial increase of the potential radius would allow for a reproduction of the data comparable to SM and IBA-2. However, the structure of the ^{94}Mo ground state with only two valence protons in the $1g_{9/2}$ shell does not leave much room for a modification of the proton mean-field parameters with the constraint to reproduce other quantities like empirical single-particle energies. This problem is avoided in the SM calculations by the use of effective charges normalized to the experimental transition strengths.

4.5 Two-phonon fully symmetric and mixed-symmetry states

Next, the structure of two-phonon state candidates is discussed. Figure 4.4 shows the comparison of the SM and QPM results to the corresponding (e,e′) and (p,p′) data. Again, the momentum transfer dependence of the transitions to the 2_2^+ and 2_5^+ states is quite similar in the electron scattering while it differs qualitatively from that of the one-phonon states shown in Fig. 4.2. The (e,e′) form factors are sensitive to the interference of the weakly excited, but large two-phonon components with strongly excited, but small one-phonon admixtures. Here, the SM significantly overshoots the (e,e′) data on the FSS indicating too large one-phonon components in the wave function. This is indicated by large seniority-2 contributions of about 45% in the SM wave function (although they do not provide a direct measure of the one-phonon component). The QPM provides cross sections of the correct magnitude although it predicts a pronounced minimum at a momentum transfer $q \simeq 0.72$ fm^{-1} due to an interference of the main two-phonon component

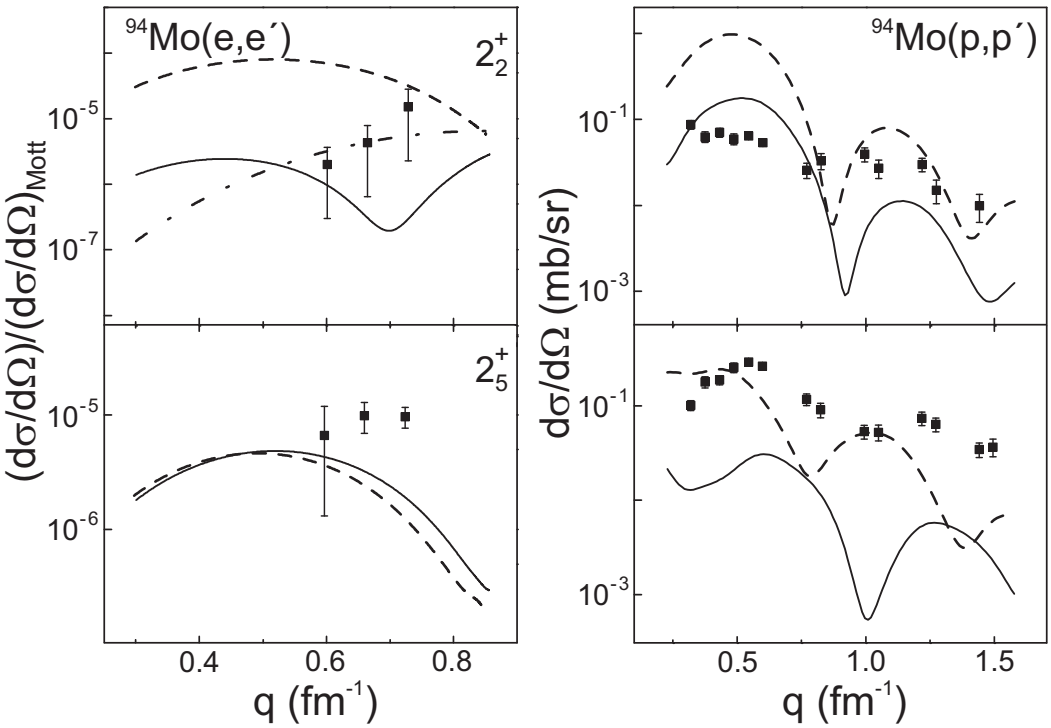

Fig. 4.4: Momentum-transfer dependence of the two-phonon FSS (top) and MSS (bottom) excitation strengths in ^{94}Mo. Left: electron scattering. Right: proton scattering. The data (full squares) are compared to QPM (solid lines), SM (dashed lines), and simplified (pure) QPM (dashed-dotted lines) calculations described in the text.

(81%) with a (19%) admixture of the 2_4^+ state. Because of its dominant neutron configuration ($2d_{5/2}^{-1}3s_{1/2}$), the overall contribution to the (e,e′) cross sections is small. In the simplified QPM calculations discussed above (considering the basic one- and two-phonon states only) a good description is achieved. This indicates that the symmetric two-phonon state is very pure; more pure than the full QPM can quantitatively predict.

For the MSS, the SM and the full QPM results are very similar. The theoretical results are somewhat smaller than the data but account roughly for the momentum transfer dependence. An increase of the predicted one-phonon admixtures of about 3% to 8 – 15% (depending on the assumed configuration) would lead to a quantitative agreement with experiment. In any case, a dominant two-phonon character prevails.

As is visible on the r.h.s. of Fig. 4.4, both SM and QPM results fail to describe

the (p,p′) results for both two-phonon 2^+ states. A possible explanation is the neglect of two-step processes in the (p,p′) reaction mechanism. Such contributions are small for collective transitions at a beam energy of 200 MeV but are important [67] for the extreme case of very weak one-step excitations and strong two-step excitations through collective levels encountered here.

4.5.1 Coupled-channel analysis

To estimate the two-step processes at least qualitatively, a coupled-channel analysis was performed with the code CHUCK3 [68]. It is based on the collective model describing nuclear excitations as surface vibrations of multipolarity L, whose amplitude is proportional to a coupling strength c_L, which is defined as the ratio of the experimental to the calculated cross section

$$c_L^2 = \left(\frac{d\sigma}{d\Omega}\right)_L^{exp} \Bigg/ \left(\frac{d\sigma}{d\Omega}\right)_L^{DWBA} . \tag{4.7}$$

This approximation is insensitive to the isospin nature of the transitions to the one-phonon states. The only requirement is collectivity demonstrated above for the case of ^{94}Mo.

Tab. 4.2: Parameters of the optical potential for the description of the incoming and outgoing protons for the ^{94}Mo(p,p′) reaction at 200 MeV used for the coupled-channel analysis.

	Woods-Saxon potential			*LS* potential		
	V, MeV	r, fm	a, fm	V, MeV	r, fm	a, fm
Re	17.520	1.257	0.750	-2.484	1.021	0.787
Im	-10.980	1.253	0.822	1.853	1.020	0.592

Starting from the global set of Ref. [69], optical model parameters for the description of the incoming and outgoing protons for the ^{94}Mo(p,p′) reaction at 200 MeV were determined by a fit to the elastic scattering cross sections and are listed in Tab. 4.2.

The transition potential was taken to be the derivative of the optical potential. In the calculations the same set of parameters has been used for the description of the distorted waves (Tab. 4.2) and of the transition potential. Only the diffuseness of the real part of the Woods-Saxon potential for the transition to the 2_3^+ state and of the imaginary part of the Woods-Saxon and LS potential for the all transitions have been adjusted to 0.3 fm to reproduce the momentum-transfer dependence of the transitions to the one-phonon 2_1^+ and 2_3^+ states.

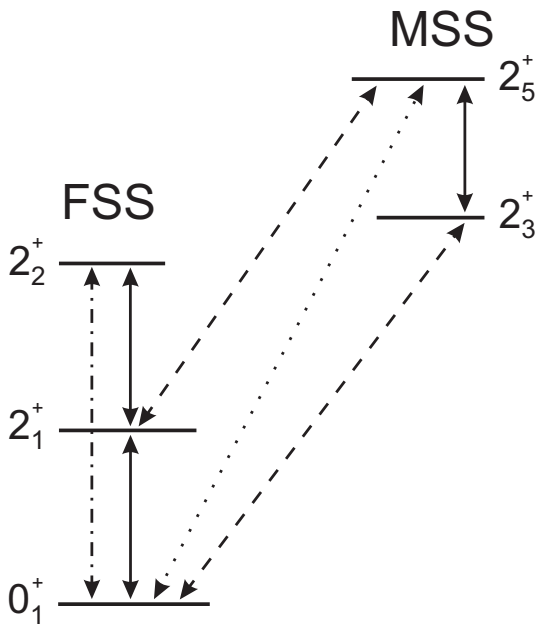

Fig. 4.5: Coupled-channel scheme for the excitation of the one- and two-phonon FSS (left) and MSS (right) in the ^{94}Mo(p,p$'$) experiment.

Figure 4.5 shows the coupling schemes taken into account for the one- and two-phonon FSS (left) and MSS (right), respectively. The coupling strengths of the one-phonon transitions to the 2_1^+ and 2_3^+ states were determined by a fit to the data. These results are displayed on the l.h.s. of Fig. 4.6. The best descriptions of the one-phonon FSS and MSS were obtained for $c_2 = 1.23$ and 0.35, respectively. For the calculation of the transitions to the two-phonon states, unknown (like $2_1^+ \rightarrow 2_5^+$) or poorly known (like $2_1^+ \rightarrow 2_2^+$) transition strengths [13] were fixed assuming harmonic vibrations.

The CHUCK3 results for the two-phonon states are displayed on the r.h.s. of Fig. 4.6. The best description of the 2_2^+ state is achieved for a vanishing one-step

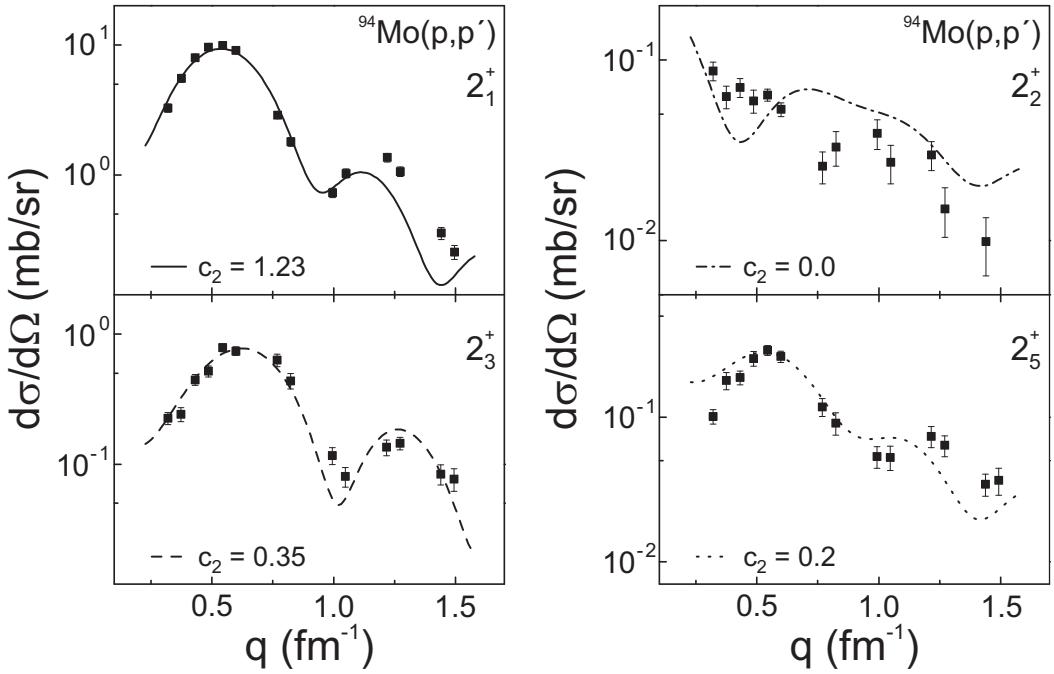

Fig. 4.6: Coupled-channel analysis for the excitation of the one- and two-phonon FSS and MSS in the ^{94}Mo(p,p′) experiment. Left: Best fits to the data (solid and dashed lines, respectively) using coupling strengths $c_2 = 1.23$ and 0.35 for the transitions to the one-phonon FSS (top) and to the MSS (bottom), respectively. Right: Best fits to the data (dashed-dotted and dotted lines, respectively) using coupling strengths $c_2 = 0.0$ and 0.2 for the transitions to the FSS (top) and to the MSS (bottom), respectively.

amplitude ($c_2 = 0.0$), *i.e.*, the cross sections are explained by two-step processes entirely. This in turn confirms the conclusion of a nearly pure two-phonon nature already drawn from the electron scattering results. A value of $c_2 = 0.2$ is obtained for the transition to the 2^+_5 state. The corresponding one-step cross section implies a one-phonon component roughly (the exact value is sensitive to possible anharmonicities and optical model parameters) in accord with the estimate obtained from the (e,e′) results. Thus, after consideration of two-step contributions to the (p,p′) cross sections a consistent picture is obtained with both experimental probes: The one-phonon components of the predominant two-phonon states are $< 10\%$ for the FSS and 8 - 15% for the MSS. In both cases they are small indeed.

5 Summary and outlook

The nature of one- and two-phonon symmetric and mixed-symmetric 2^+ states in ^{94}Mo have been tested for the first time through high energy-resolution inelastic electron and proton scattering experiments in a combined analysis. Results from QPM, SM and IBM-2 calculations confirm the dominant one-phonon structure of the transitions to the first and third 2^+ state.

In contrast to electron scattering, where the proton component of the nuclear wave function is excited only, in proton scattering both electron and proton components contribute. Thus, the combined data reveal the isovector character of the transition to the one-phonon MSS within the valence shell by their different momentum-transfer dependence and the analysis of the microscopic wave functions.

Excitation of the two-phonon states is sensitive to admixtures of one-phonon components, which are found to be small. Consistent estimates of one-phonon admixtures are obtained from both experimental probes when two-step contributions to the proton scattering cross sections are taken into account.

Clearly, the combination of electromagnetic and hadronic scattering is a versatile tool for detailed studies of nuclear wave functions. This work opens a new experimental avenue for future investigations of MSSs. One obvious application would be the study of ^{92}Zr. Its structure is particularly interesting because it lies at the proton subshell closure $Z = 40$, and strong shell effects are expected to influence in the properties of the collective one-phonon states [16, 70]. It is planned to investigate the structure of this nucleus with the high-resolution electron and proton scattering experiments also. Proton scattering experiments have already been performed at the iThemba LABS; a ^{92}Zr(p,p$'$) spectrum measured with 200 MeV protons at 6° is presented in Fig. 5.1. The electron scattering experiments will be carried out during a forthcoming beam time at the S-DALINAC.

It would be also very interesting to investigate the mixed-symmetry structure of the ^{94}Zr nucleus, where for the first time, the $B(E2; 2^+_{1,MSS} \rightarrow 0^+_1)$ is observed [71] to be larger than $B(E2; 2^+_{1,FSS} \rightarrow 0^+_1)$.

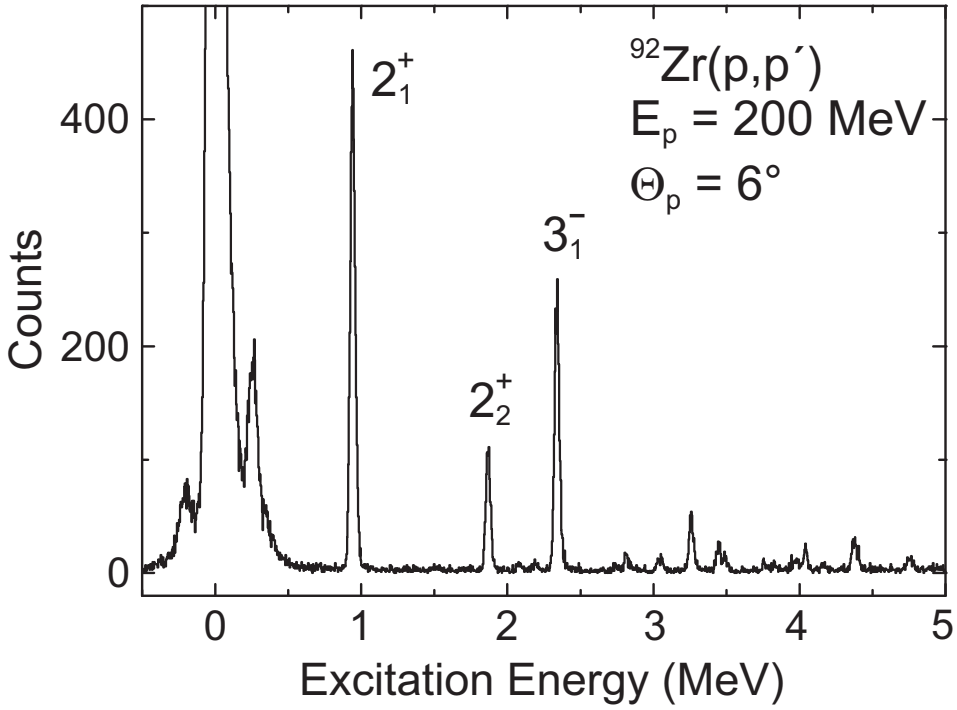

Fig. 5.1: Spectrum of the ^{92}Zr(p,p′) reaction measured with 200 MeV protons at a scattering angle of 6° at iThemba LABS.

PART II:
Line Shape of the First Excited $1/2^+$ State in ^{9}Be

6 Introduction

The recent renewed interest in very light nuclei due to the progress in *ab initio* calculations applied to their structure, now capable to describe their properties up to mass number $A \approx 12$ [72]. The low-energy level structure (see Fig. 6.1) of the ^{9}Be nucleus has long been a matter of interest, in particular with respect to the strength of three-body $\alpha + \alpha + n$ cluster configurations.

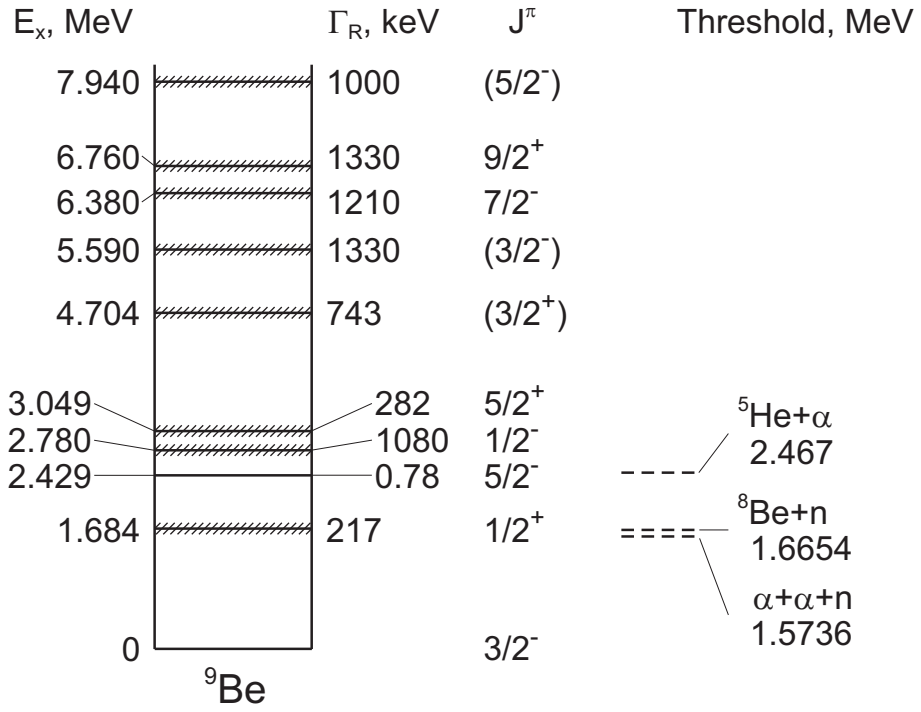

Fig. 6.1: The low-lying excited states in ^{9}Be with corresponding energies, intrinsic widths and possible decay channels (adopted from [73]).

In neutron-rich astrophysical environments, such as core-collapse supernovae, the three-body reaction $\alpha + \alpha + n \rightarrow {}^9$Be followed by $^9\mathrm{Be}(\alpha, n)^{12}\mathrm{C}$ may provide a route for building up the heavy elements and triggering the r-process [74–77].

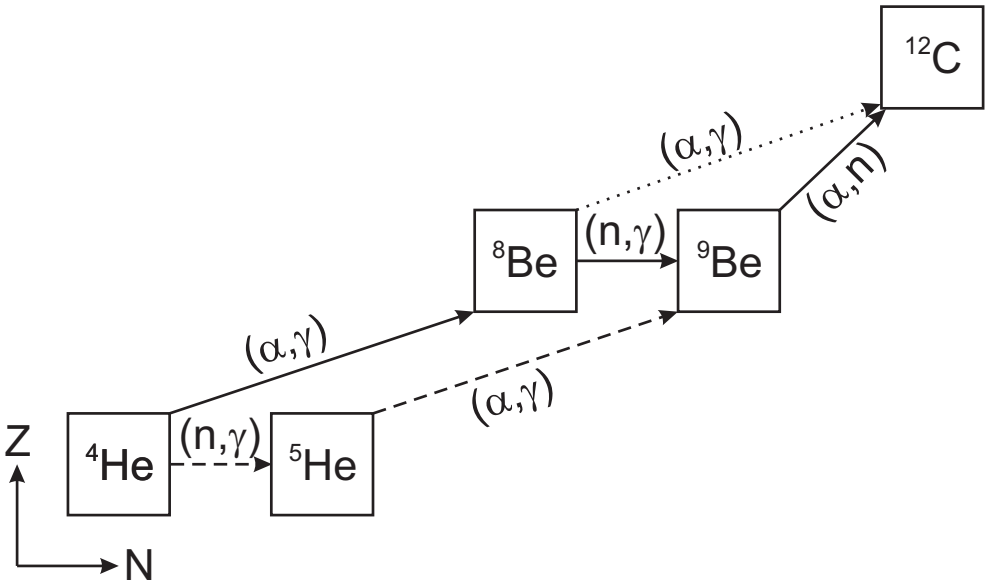

Fig. 6.2: Possible production chains of ^{12}C.

Figure 6.2 shows possible production chains of ^{12}C. The first stage can proceed mainly by two routes, either $\alpha + \alpha \rightarrow {}^8\mathrm{Be}$ followed by ${}^8\mathrm{Be} + n \rightarrow {}^9\mathrm{Be}$ (solid line), or $\alpha + n \rightarrow {}^5\mathrm{He}$ followed by ${}^5\mathrm{He} + \alpha \rightarrow {}^9\mathrm{Be}$ (dashed line). Triple α-process (dotted line) for the production of ^{12}C, which dominates in stellar burning, can be neglected in explosive nucleosynthesis because of the short time scales. In the absence of any experimental evidence for the ${}^5\mathrm{He} + \alpha$ configuration, calculations are generally performed assuming the ${}^8\mathrm{Be} + n$ route only, the argument being that the different lifetimes of the ^{8}Be and ^{5}He intermediate states (10^{-16} s and 10^{-21} s, respectively) should favour the former. For example, this has recently been studied for the second excited state at $E_x = 2.429$ MeV, but remains unknown for other transitions. However, calculating the rate properly requires a knowledge of the relative importance of ${}^8\mathrm{Be} + n$ and ${}^5\mathrm{He} + \alpha$ cluster configurations in ^{9}Be.

The key states in this context are those just above the particle threshold, in particular the first excited state at $E_x = 1.684$ MeV ($J^\pi = 1/2^+$), see Fig. 6.1. The description of this unbound level, its resonance energy and width is a long-standing problem. Due to its closeness to the ${}^8\mathrm{Be} + n$ threshold the resonance has a strongly asymmetric line shape.

Many experiments have investigated the ${}^9\mathrm{Be}(\gamma, n\alpha){}^4\mathrm{He}$ reaction, either with real photons from bremsstrahlung or from laser-induced Compton backscattering, or

with virtual photons from electron scattering (see Ref. [73] for a discussion and references). But despite a large number of different experiments there still exist considerable uncertainties of the resonance parameters. In the work of Utsonomiya *et al.* [78] the photoneutron cross section for ^{9}Be was measured with real photons in the whole energy range of astrophysical relevance. Electromagnetic quantities for ^{9}Be were deduced by a least-squares analysis of the data within the Breit-Wigner formalism. The best-fit resonance parameters for the $1/2^+$ state are summarized in Tab. 6.1 in comparison with results from earlier electron scattering experiments [79, 80].

Tab. 6.1: Resonance parameters and reduced transition probability of the $1/2^+$ state in ^{9}Be deduced from different experiments.

	Real photon exp.	(e,e′)		Reanalysis of [79]
	Ref. [78]	Ref. [79]	Ref. [80]	by Barker [82]
E_R, MeV	1.75(1)	1.684(7)	1.68(15)	1.7316
Γ_R, keV	283(42)	217(10)	200(20)	280
$B(E1)\uparrow$, e^{2}fm^2	0.0535(35)	0.027(2)	0.034(3)	0.0685

Obviously there are significant differences between resonance properties deduced from the photonuclear and the electron scattering experiments. The discrepancy in the $B(E1)$ transition strength amounts to a factor of 2 when comparing with the results of the earlier (e,e′) experiments [79, 81], while it is reduced to $\sim 30\%$ by the later (e,e′) experiment [80]. The reason for these discrepancies between the real photon experiment and virtual photon remains still unknown. Barker [82] has reanalysed previously measured (e,e′) data of Küchler *et al.* [79]. The parameter values obtained ($E_R = 1.7316$ MeV, $\Gamma_R = 280$ keV, $B(E1)\uparrow = 0.0685$ e^{2}fm^2) differ considerably from those of [79].

In order to resolve these discrepancies, in the present work new high-resolution ^{9}Be(e,e′) experiments were performed at the S-DALINAC and an independent reanalysis of the electron scattering data [79] is presented.

7 Description of excited states in the continuum

In the present work, R-matrix theory in one-level approximation is used to deduce the resonance parameters. In scattering experiments above the particle thresholds in addition to the scattered particles one or several reaction products have to be considered in the final state. The cross section for such a reaction is of the type

$$A + a \rightarrow B^* \rightarrow \begin{cases} C + c \\ D + d \\ \dots \end{cases}, \tag{7.1}$$

in which the nucleus B is formed in a state unstable to particle emission. Assuming only one decay channel $C + c$, the cross section giving the energy distribution of particle c can be expressed as

$$\sigma(E_B) = const \cdot \left| \left\langle C + c \,|\, \hat{O} \,|\, A + a \right\rangle \right|^2 \cdot \rho(E_B). \tag{7.2}$$

In addition to the matrix element of the transition operator $\hat{O}$ the energy dependence of the cross section is described by the density-of-state function $\rho(E_B)$ of the nucleus B, providing the probability to form B with excitation energy E_B [83].

According to Breit and Wigner [84], the contribution to the cross section from a level of spin J, in the one-level approximation of R-matrix theory [83] is given by

$$\sigma_{a,c}(E) = \frac{\pi}{2\,k_a^2}\, g_J\, \frac{\Gamma_a\, \Gamma_c}{(E - E_\lambda - \Delta(E))^2 + \frac{\Gamma^2}{4}}. \tag{7.3}$$

The quantities Γ_a and Γ_c denote the partial decay widths and Γ the total width, E_λ corresponds to the energy eigenvalue, and to k_a the wave number of the incoming particle a. The level shift $\Delta(E)$ is given by

$$\Delta(E) = -\gamma^2\,(S(E) - B_n), \tag{7.4}$$

with the reduced width γ^2, the shift factor $S(E)$ and the boundary condition parameter B_n (see Ref. [83]). The spin statistical factor g_J is defined as

$$g_J = \frac{2J + 1}{2I + 1}, \tag{7.5}$$

where I, J are the total angular momenta of initial and compound nucleus, respectively.

In the case of a photoabsorption process followed by neutron decay the photon corresponds to particle a, the target nucleus is A, neutron c, and the rest nucleus C. Thus, the (γ, n) cross section for the excitation of an isolated level near threshold can be written as

$$\sigma_{\gamma,n}(E_\gamma) = \frac{\pi}{2\,k_\gamma^2}\,g_J\,\frac{\Gamma_\gamma\,\Gamma_n}{(E_\gamma - E_\lambda - \Delta)^2 + \frac{\Gamma^2}{4}}, \tag{7.6}$$

where $k_\gamma = E_\gamma/\hbar c$ stands for the photon wave number, Γ_γ for the ground state radiative width, Γ_n for the neutron decay width, and the total decay width $\Gamma = \Gamma_\gamma + \Gamma_n$.

Then for $1/2^+$ level in ^{9}Be excited by $E1$ γ-radiation and decaying by s-wave neutrons, and for an energy $E = E_\gamma - S_n > 0$ (with the neutron threshold energy $S_n(^9\mathrm{Be}) = 1.6654$ MeV), one has

$$\Gamma_\gamma = \frac{16\,\pi}{9}\,e^2\,k_\gamma^3\,B(E1,k)\!\downarrow, \tag{7.7}$$

$$\Gamma_n = 2\,\sqrt{\epsilon\,(E_\gamma - S_n)}, \tag{7.8}$$

$$\Delta = 0, \tag{7.9}$$

with $B(E1,k)\downarrow$ being the reduced transition strength at the photon point for the decay, $\epsilon = 2\,\mu\,a^2\,\gamma^4/\hbar^2 > 0$, where μ, a are the reduced mass and channel radius for the $^8\mathrm{Be} + n$ channel, respectively. Calculating the energy shift Δ (see Eq. (6.1)), the boundary condition parameter B_n is taken to be zero and the shift factor $S(E) = 0$ for s-wave neutrons [83]. Thus, on the low energy side the originally symmetric Breit-Wigner line is modified and shows a steep rise up to maximum. On the high energy side the resonance follows the Breit-Wigner form of Eq. (7.6).

Since $\Gamma_n \gg \Gamma_\gamma$, the total resonance width $\Gamma \approx \Gamma_n$ and the energy dependence of the photoabsorbtion cross section of Eq. (7.6) is given by

$$\sigma_{\gamma,n}(E_\gamma) = \frac{16\,\pi^2}{9}\,\frac{e^2}{\hbar c}\,g_J\,B(E1,k)\!\downarrow\,\frac{E_\gamma\,\sqrt{\epsilon\,(E_\gamma - S_n)}}{(E_\gamma - E_R)^2 + \epsilon\,(E_\gamma - S_n)}, \tag{7.10}$$

Resonance levels occur at energies E_R which fulfil the condition $E_R - E_\lambda - \Delta_n = 0$. Thus, the resonance energy is defined as

$$E_R = E_\lambda + \Delta(E_R), \tag{7.11}$$

and the resonance width using Eq. (7.8)

$$\Gamma_R(E_R) = 2\sqrt{\epsilon(E_R - S_n)}. \tag{7.12}$$

It should be noted that in the present case the resonance energy E_R does not coincide with the energy at the maximum of the cross section, and the resonance width Γ_R and FWHM are not the same.

If there is no further open channel near threshold, one can find a relationship between the $\sigma_{\gamma,n}$ cross section and those measured in the electron scattering $\sigma_{e,e'}$ by extrapolating the reduced transition strength $B(E1,q)$ at finite momentum transfer q to that at the photon point, *i.e.* $B(E1,k)$. For not too large ($\Gamma < 1$ MeV) widths, the momentum transfer varies little over the resonance and the e,e$'$) cross sections as a function of the excitation energy E_x in the excited nucleus can be written as

$$\sigma_{e,e'}(E_x) = \frac{16\,\pi^2}{9}\,\frac{e^2}{\hbar c}\,B(E1,q)\uparrow\;\frac{E_x\,\sqrt{\epsilon\,(E_x - S_n)}}{(E_x - E_R)^2 + \epsilon\,(E_x - S_n)}, \tag{7.13}$$

with $B(E1,q)\uparrow$ being the reduced transition for the excitation, which is connected to that for the decay through $B(E1,q)\uparrow = g_J\,B(E1,q)\downarrow$. Note that Eq. (7.13) is defined for $E_x > S_n$ only.

In the Plane Wave Born Approximation (PWBA) appropriate for light nuclei and low momentum transfers an extrapolation of the reduced transition strength to the photon point provides a connection between $B(E1,k)$ and $B(E1,q)$ with the help of the so-called transition radius R_{tr} [85]

$$\sqrt{B(C1,q)} = \sqrt{B(C1,k)}\,\left(1 - q^2\,\frac{R_{tr}^2}{10} + q^4\,\frac{R_{tr}^4}{280} - \ldots\right). \tag{7.14}$$

Assuming validity of the Siegert theorem, $B(E1,q) = (k/q)^2\,B(C1,q)$, one can extract $B(E1,k)$.

8 Results and discussion

8.1 Experiments

The ^{9}Be(e,e′) experiment was carried out at the high-resolution 169° magnetic spectrometer of the S-DALINAC. Data were taken at an incident electron beam energy $E_e = 73$ MeV and scattering angles $\Theta_e = 93°$ and 141° with typical beam currents of 2 μA. For the measurements a self-supporting ^{9}Be target with an areal density of 5.55 mg/cm^2 was used. In dispersion-matching mode an energy resolution $\Delta E \simeq 30$ keV (FWHM) was achieved.

As already discussed in Sec. 3.1.2 due to the limited spectrometer momentum acceptance of only about 4% an excitation energy region of about 2.92 MeV is covered only at an incident electron beam energy of 73 MeV. To extract an excited spectrum up to about 8 MeV separate spectra were measured at different magnetic field settings, calibrated using well known prominent excitations of $J^\pi = 0^+, 2^+, 3^-$ states up to $E_x = 8$ MeV in ^{12}C [86] and ^{28}Si [87], reduced to the same energy bin size, and then sewed together.

Figure 8.1 presents the spectra of the ^{9}Be(e,e′) reaction measured at scattering angles of 93° (top) and 141° (bottom). There are only two narrow peaks visible. The first one is the elastic line and the second one corresponds to the excitation of the $5/2^-$ state at $E_x = 2.429$ MeV. The tiny peaks at about 4.2 MeV correspond to the second excited state in ^{12}C ($E_x = 4.439$ MeV). The bumps around 5.1 MeV in the top spectrum and around 8.1 MeV in the bottom spectrum are due to elastic scattering on hydrogen. The broad bump between 6 and 7 MeV is shown to correspond to the states at $E_x = 6.38$ MeV ($J^\pi = 7/2^-$) and $E_x = 6.76$ MeV ($J^\pi = 9/2^+$) in ^{9}Be [80]. The asymmetric line shape of the $1/2^+$ state at $E_x = 1.684$ MeV is already clearly visible without background subtraction.

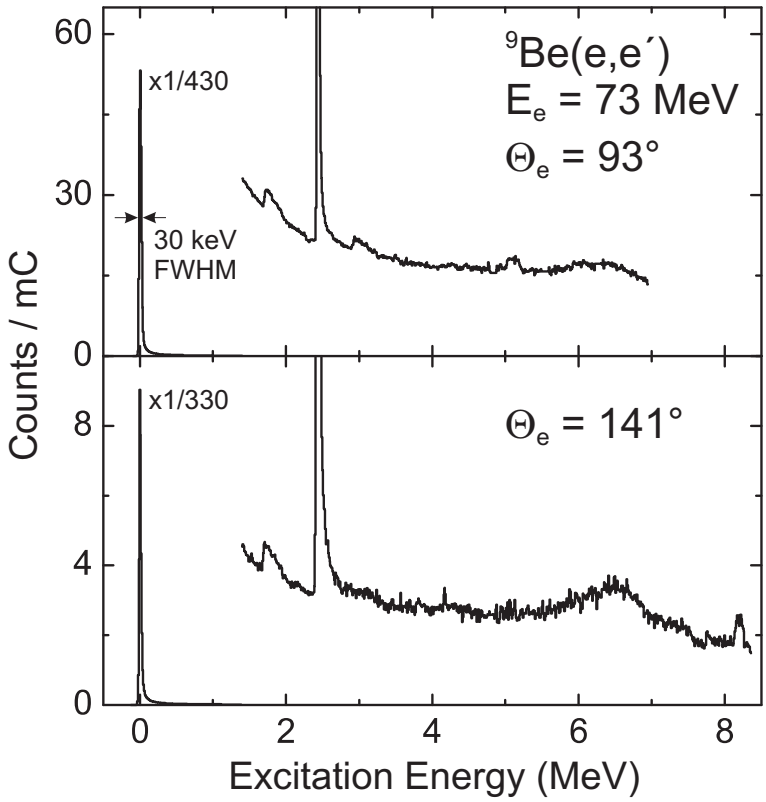

Fig. 8.1: ^{9}Be(e,e′) spectra measured at $E_e = 73$ MeV and $\Theta_e = 93°$ and 141°.

8.2 Decomposition of the spectra

During the experiments it was observed that some strips of the new focal plane detector [36] have become noisy influencing the detector efficiency. It is known that the ^{12}C(e,e′) spectrum above an excitation energy of 30 MeV has no structure and no resonances, and can thus serve as a "white" spectrum. The result of such a measurement is shown in Fig. 8.2. The dashed line is a mean value deduced from detectors 1, 2 and 4. The efficiency over the detection modules assuming a Gaussian distribution is found to be constant within a 2σ band (dotted lines) except for the third detector module.

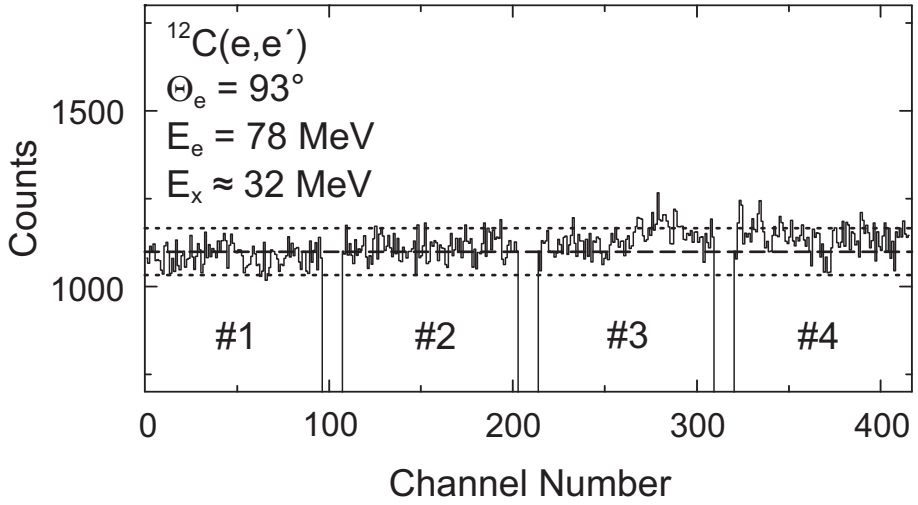

Fig. 8.2: Spectrum of ^{12}C(e,e′) reaction at $E_e = 78$ MeV, $\Theta_e = 93°$ and $E_x \approx 32$ MeV used as a check of relative efficiency. The dashed line is the mean value deduced from detectors 1, 2 and 4. The efficiency along the detection modules assuming a Gaussian distribution is seen to be constant within a 2σ band (dotted lines) except for the third detector module.

For the measurements of strongly excited transitions this effect can be neglected, but not in the case of very weak excitations as in the present case. Especially, since one wants to determine the line shape of the resonance, the spectra need to be corrected. For that purpose a spectrum of the ^{12}C(e,e′) reaction measured in the same kinematics as one of the ^{9}Be data sets was used as shown on the l.h.s. of Fig. 8.3.

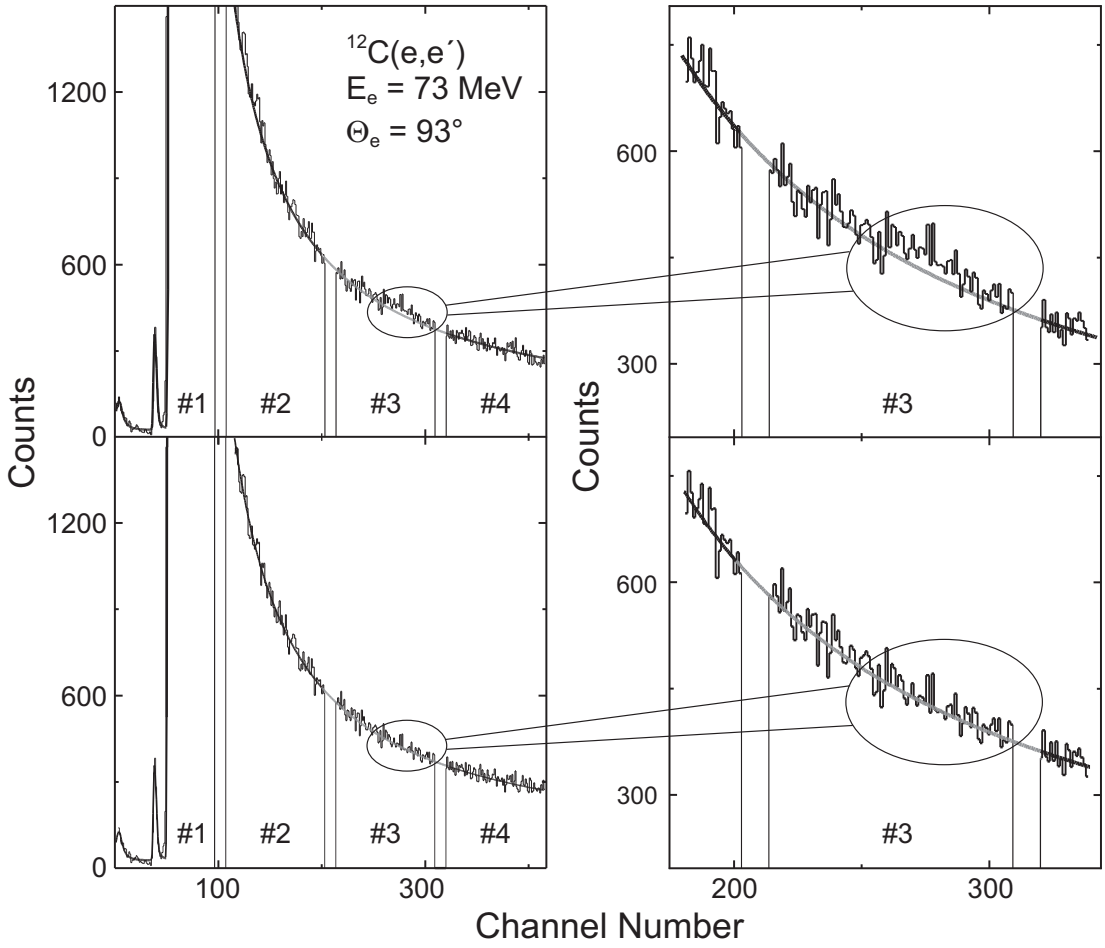

Fig. 8.3: Spectrum of ^{12}C(e,e′) reaction at E_e = 73 MeV and Θ = 93°. Top: Original spectrum. The solid line is a fit of the radiative tail of elastic scattering excluding the third detector module. It is seen that the region marked with an oval (enlarged in the insets on the r.h.s.) in the third detector module systematically too high. Bottom: Corrected spectrum with an extended view (on the r.h.s.) on the relevant region.

The spectrum covers an excitation energy region from $E_x = 0 - 3$ MeV. The solid line corresponds to a fit of the radiative tail of the elastic line in the interval excluding the third detector module. An extended view (inset on the r.h.s. of Fig. 8.3) clearly shows that within the third detector module there is a region where the microstrips are too "noisy". Except for the elastic line no other excitations are expected. Therefore, count rates in that region have to be corrected. The correction factor can be defined as a ratio of the fit function and the experimental spectrum. In this case the correction depends on the statistics of the

reference spectrum. To remove the statistical fluctuations the correction factor was smoothed with a Gaussian function. The corrected spectrum is presented on the l.h.s. of Fig. 8.3 (bottom) with the extended view on the r.h.s. The same correction procedure was applied to the ^{9}Be(e,e$'$) spectra.

A decomposition of ^{9}Be(e,e$'$) spectra into a background from the radiative tail and resonance contributions, taking into account all states of Fig. 6.1 performed using the programm FIT [42]. The line shape of the narrow states was described by the function given in Eq. (3.1) and the line shape of the broad resonances by the modified Breit-Wigner function of Eq. (7.13). The positions and widths of the resonances (taken from the last compilation [73]) were kept fixed during the fit except for the parameters of the elastic line and the first inelastic state. The results of the decomposition are shown in Fig. 8.4.

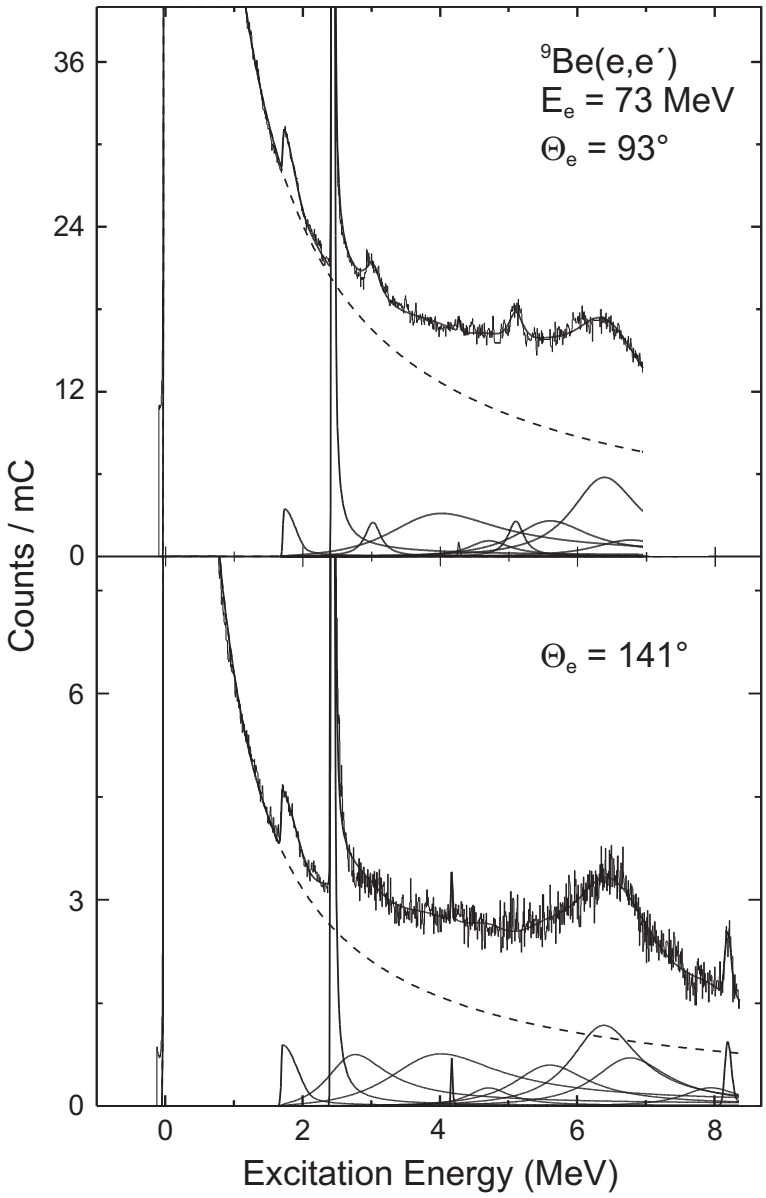

Fig. 8.4: Spectra of the ^{9}Be(e,e′) reaction at E_e = 73 MeV and Θ_e = 93° (top) and 141° (bottom) and their decomposition. Solid lines: Experimentally known resonances and fit (see Fig. 6.1). Dashed lines: Radiative tail from elastic scattering.

8.3 Extraction of the $B(E1)$ transition strength

Absolute differential cross sections for the $1/2^+$ state where determined from the area contents corrected for the radiation effects using the procedure described in Sec. 3.1.3. The $B(E1)$ transition strength at the photon point was extracted from the experimental data using two independent ways. The first method is model independent. In PWBA one can extract the reduced transition strength at photon point k using Eq. (7.14).

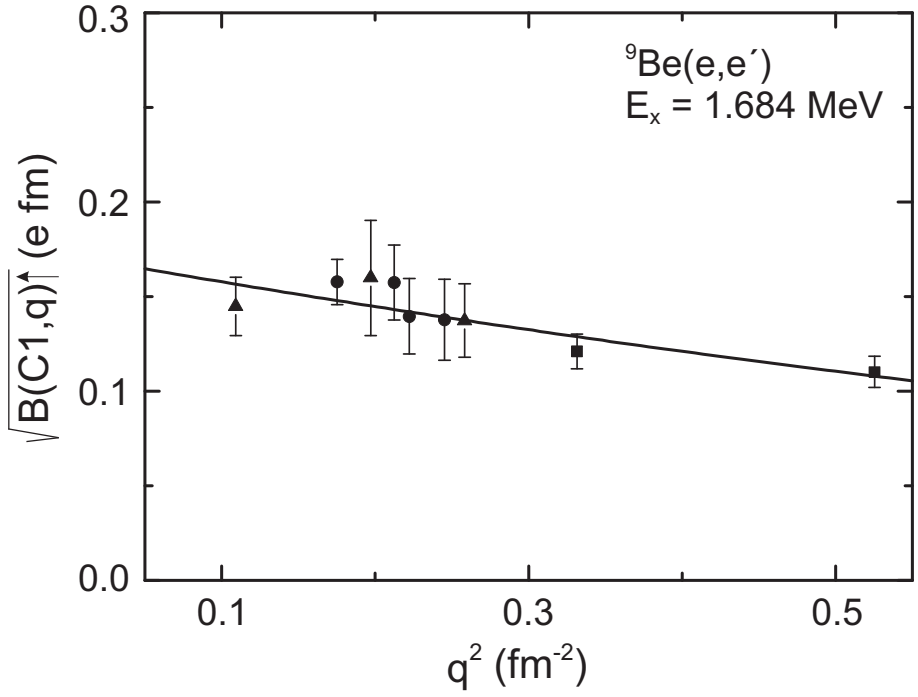

Fig. 8.5: Extrapolation of the reduced transition probability to the photon point. Data are from Ref. [81] (triangles), Ref. [79] (circles) and present work (squares).

Figures 8.5 presents the old data measured at low momentum transfer together with the present data using Eq. (7.14). The solid line shows a fit of the data resulting in the $B(E1,k)\uparrow = 0.027(4)\,\mathrm{e^2fm^2}$ and the transition radius $R_{tr} = 2.9(3)$ fm, which agrees with the result already published in Ref. [79].

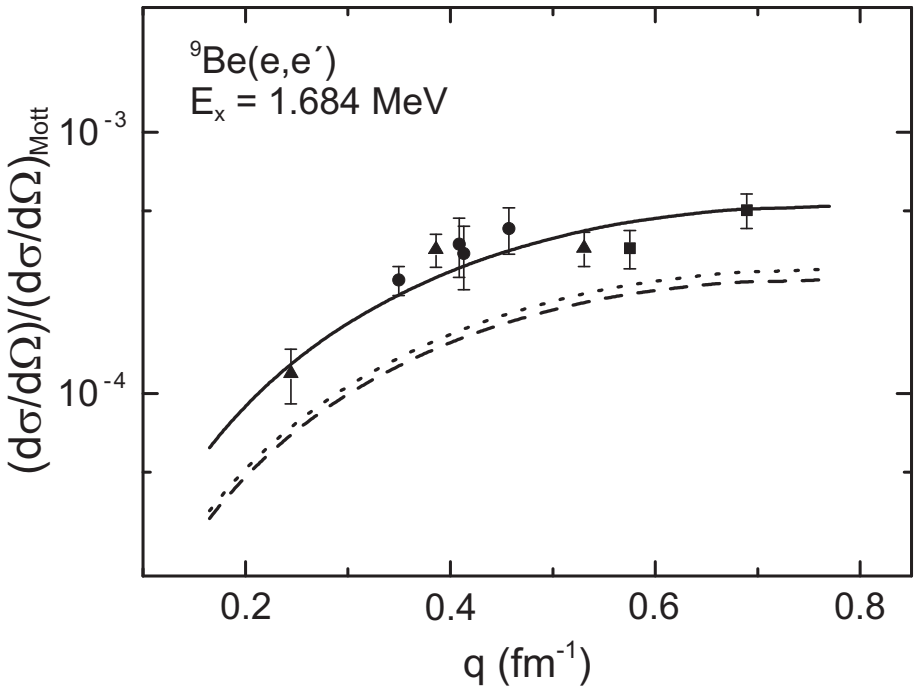

Fig. 8.6: Comparison of the measured form factor of the $1/2^+$ state in ^{9}Be with NCSM calculations in different model spaces. The dashed line corresponds to a (4 – 5) $\hbar\Omega$ model space, the dotted line to a (6 – 7) $\hbar\Omega$ model space. The solid line is the best fit on the experimental data.

The $B(E1,k)$ transition strength can be also determined by fitting the experimental data using a theoretically calculated momentum-transfer dependence of the form factor. Figure 8.6 presents the momentum transfer dependence of the (e,e′) cross section normalized to the Mott cross section for the transition to the first excited state in ^{9}Be. The experimental data are compared to a no-core shell model calculation (NCSM) [88–91]. In this *ab initio* approach one starts from a realistic nucleon-nucleon potential and solves the A-body problem, producing an antisymmetrized total wave function. Here there is no closed shell core, meaning that all nucleons are active as compared to the usual shell model calculations (already discussed in Sec. 4.1.1), where only valence nucleons are taken into account. At present time the computer processing power limits the NCSM calculations in $A = 9$ nuclei to model spaces up to about 8 $\hbar\Omega$. Figure 8.6 also shows NCSM results with model spaces of 4 – 5 $\hbar\Omega$ (dashed line) and 6 – 7 $\hbar\Omega$ (dotted line) which predict the $B(E1,k)\uparrow = 0.0145$ e^{2}fm^2 and 0.0155 e^{2}fm^2, respectively. It is seen that the model space is not yet sufficient to reproduce the experimental

$B(E1)$ transition strength, *i.e.* the calculations are not yet converged. A fit on the experimental data (solid line) gives $B(E1,k)\uparrow = 0.027(3)\,\mathrm{e^2fm^2}$ in agreement with the result obtained from the PWBA analysis.

8.4 Extraction of the ^{9}Be(γ,n) cross sections

Subtracting all contributions from other resonances and from the elastic line, one can convert (e,e′) cross sections to the (γ, n) cross sections using Eq. (7.10) and the extracted $B(E1,k)$ transition strength at the photon point. Figure 8.7 shows the results and a fit using Eq. (7.10) folded with the instrumental resolution function to reproduce the line shape. The two upper graphs correspond to the present measurements. The bottom graph displays the old (e,e′) data from [79] and their reanalysis. The results of the fits are summarized in the Tab. 8.1. The resonance energies and widths of the spectra are close but differ by slightly more then 1σ. Reanalysis of [79] shows parameters in agreement with the new data and differ from those published in [79].

Tab. 8.1: Line shape parameters of the $1/2^+$ state in ^{9}Be obtained from the present data and a reanalysis of older (e,e′) data [79].

	present data		old data [79]
	73 MeV, 93°	73 MeV, 141°	49 MeV, 117°
E_R, MeV	1.746(8)	1.768(12)	1.737(10)
Γ_R, keV	265(10)	308(20)	275(14)

Since all three measurements are independent, the data can be averaged and then reanalysed. The resulting (γ, n) cross sections and fit are presented on Fig. 8.8. The fit results in a resonance energy $E_R = 1.748(6)$ MeV and a width $\Gamma_R = 274(8)$ keV in agreement with the results obtained from the latest real photon experiments [78].

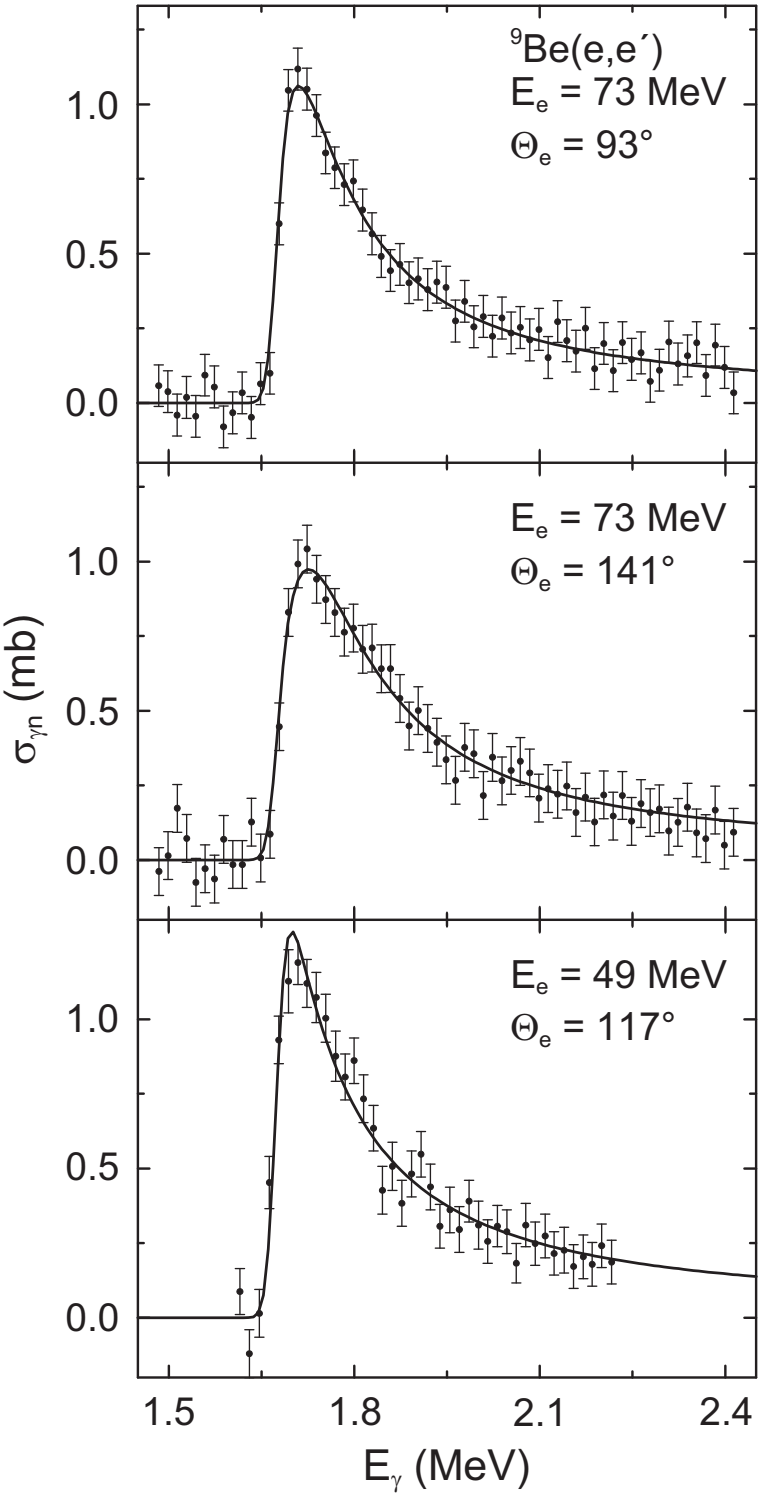

Fig. 8.7: Photoneutron cross section extracted from the (e,e′) present (top and middle) and older (bottom) experiments [79]. The solid lines correspond to a fit with the modified Breit-Wigner function of Eq. (7.10) folded with the experimental resolution function. Fit parameters are given in Tab. 8.1.

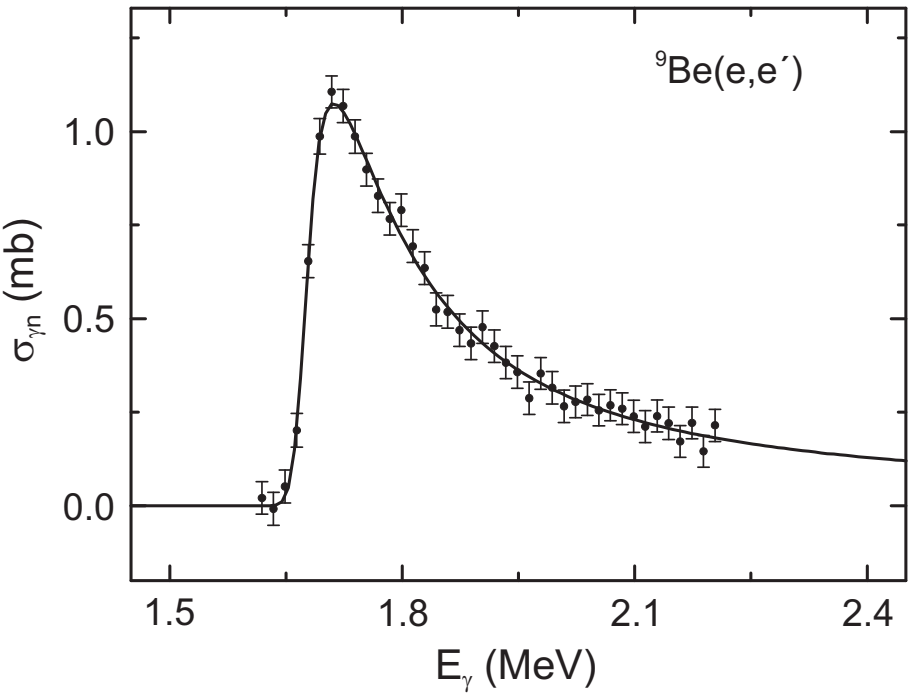

Fig. 8.8: Averaged photoneutron cross sections extracted from the (e,e′) data shown in Fig. 8.7. The solid line is a fit with the modified Breit-Wigner function of Eq. (7.10) folded with the experimental resolution function.

8.5 Astrophysical implications

The rate of the astrophysically relevant reaction chain ^{4}He$(\alpha,\gamma)^8$Be$(n,\gamma)^9$Be can be calculated with the resonance parameters obtained in the present work. For temperatures $T_9 = 0.1$ – 3 (in units of 10^9 K) the rate is determined almost exclusively of the cross sections at $1/2^+$ resonance in ^{9}Be. At larger temperatures higher-lying resonances in ^{9}Be start to contribute. Compared to the latest compilation of astrophysical important cross sections between light nuclei [92] the present results suggest values about 20% smaller at $T_9 = 0.1$ but is about 15% larger at $T_9 = 10$ with a roughly linear increase in between. Correspondingly revised rates should be used in future astrophysical network calculations.

9 Summary

Spectra of the ^{9}Be(e,e′) reaction have been measured at the S-DALINAC at an electron energy $E_0 = 73$ MeV and scattering angles of 93° and 141° with high-energy resolution up to excitation energies $E_x = 8$ MeV. The form factor of the first excited state has been extracted from the data. The momentum-transfer dependence of its form factor is well reproduced by the modern no-core shell model calculations. The astrophysical relevant ^{9}Be(γ, n) cross sections have been extracted from the (e,e′) data. The resonance parameters of the first excited $1/2^+$ state in ^{9}Be have been derived in a one-level R-matrix approximation from the present and older [79] data. The resonance parameters averaged over these three independent measurements result in the resonance energy $E_R = 1.748(6)$ MeV and resonance width $\Gamma_R = 274(8)$ keV. These are in mutual agreement with the resonance parameters obtained from the latest real photon experiments [78]. However, the $B(E1, k)$ transition strength deduced from (e,e′) in two independent ways differs from the real photon results by a factor of two. This might be a hint that the Siegert theorem underlying this comparison is violated at the photon point for this weak transition. Such a violation might has been observed in other cases for $E1$ transitions in light nuclei before [93].

The calculation of the reaction chain ^{4}He$(\alpha, \gamma)^{8}$Be$(n, \gamma)^{9}$Be under stellar conditions shows systematic deviations as a function of temperature compared to the compilation by [92] which should be considered in future astrophysical network calculations.

References

[1] A. Bohr and B. R. Mottelson, *Nuclear structure*, Vol. 2, Benjamin, New York (1975).

[2] R. F. Casten, Nucl. Phys. **A443** (1985) 1.

[3] T. Otsuka, T. Matsuo, and D. Abe, Phys. Rev. Lett. **97** (2006) 162501.

[4] D. Bohle, A. Richter, W. Steffen, A. E. L. Dieperink, N. Lo Iudice, F. Palumbo, and O. Scholten, Phys. Lett. **137B** (1984) 27.

[5] W. Ziegler, C. Rangacharyulu, A. Richter, and C. Spieler, Phys. Rev. Lett. **65** (1990) 2515.

[6] P. von Neumann-Cosel, J. N. Ginocchio, H. Bauer, and A. Richter, Phys. Rev. Lett. **75** (1995) 4178.

[7] N. Pietralla, P. von Brentano, R.-D. Herzberg, U. Kneissl, N. Lo Iudice, H. Maser, H. H. Pitz, and A. Zilges, Phys. Rev. **C58** (1998) 184.

[8] J. Enders, P. von Neumann-Cosel, C. Rangacharyulu, and A. Richter, Phys. Rev. **C71** (2005) 014306.

[9] N. Pietralla, D. Belic, P. von Brentano, C. Fransen, R.-D. Herzberg, U. Kneissl, H. Maser, P. Matschinsky, A. Nord, T. Otsuka, H. H. Pitz, V. Werner, and I. Wiedenhöver, Phys. Rev. **C58** (1998) 58.

[10] N. Pietralla, C. Fransen, D. Belic, P. von Brentano, C. Frießner, U. Kneiss, A. Linnemann, A. Nord, H. H. Pitz, T. Otsuka, I. Schneider, V. Werner, and I. Wiedenhöver, Phys. Rev. Lett. **83** (1999) 1303.

[11] N. Pietralla, C. Fransen, P. von Brentano, A. Dewald, A. Fitzler, C. Frießner, and J. Gableske, Phys. Rev. Lett. **84** (2000) 3775.

[12] C. Fransen, N. Pietralla, P. von Brentano, A. Dewald, J. Gableskea, A. Gadea, A. Lisetskiy, and V. Werner, Phys. Lett. **B508** (2001) 219.

[13] C. Fransen, N. Pietralla, Z. Ammar, D. Bandyopadhyay, N. Boukharouba, P. von Brentano, A. Dewald, J. Gableske, A. Gade, J. Jolie, U. Kneissl, S. R. Lesher, A. F. Lisetskiy, M. T. McEllistrem, M. Merrick, H. H. Pitz, N. Warr, V. Werner, and S. W. Yates, Phys. Rev. **C67** (2003) 024307.

[14] N. Pietralla, C. J. Barton, R. Krücken, C. W. Beausang, M. A. Caprio, R. F. Casten, J. R. Cooper, A. A. Hecht, H. Newman, J. R. Novak, and N. V. Zamfir, Phys. Rev. **C64** (2001) 031301.

[15] C. Fransen, N. Pietralla, A. P. Tonchev, M. W. Ahmed, J. Chen, G. Feldman, U. Kneissl, J. Li, V. N. Litvinenko, B. Perdue, I. V. Pinayev, H. H. Pitz, R. Prior, K. Sabourov, M. Spraker, W. Tornow, H. R. Weller, V. Werner, Y. K. Wu, and S. W. Yates, Phys. Rev. **C70** (2004) 044317.

[16] C. Fransen, V. Werner, D. Bandyopadhyay, N. Boukharouba, S. R. Lesher, M. T. McEllistrem, J. Jolie, N. Pietralla, P. von Brentano, and S. W. Yates, Phys. Rev. **C71** (2005) 054304.

[17] A. Arima and F. Iachello, Phys. Rev. Lett. **35** (1975) 1069.

[18] F. Iachello, Phys. Rev. Lett. **53** (1984) 1427.

[19] T. Otsuka, A. Arima, F. Iachello, and I. Talmi, Phys. Lett. **B76** (1978) 139.

[20] F. Iachello, Nucl. Phys. **A358** (1981) 89c.

[21] N. Pietralla, P. von Brentano, R. F. Casten, T. Otsuka, and N. V. Zamfir, Phys. Rev. Lett. **73** (1994) 2962.

[22] A. Richter, *Operational experience at the S-DALINAC*, Proceedings of the Fifth European Particle Accelerator Conference, Ed. S. Meyers *et al.*, IOP Publishing, Bristol (1996) 110.

[23] P. Mohr, J. Enders, T. Hartmann, H. Kaiser, D. Schiesser, S. Schmitt, S. Volz, F. Wissel, A. Zilges, Nucl. Instr. Meth. **A423** (1999) 480.

[24] P. von Neumann-Cosel, C. Rangacharyulu, A. Richter, G. Schrieder, A. Stascheck, and S. Strauch, Phys. Rev. Lett. **78** (1997) 2924.

[25] S. Strauch, P. von Neumann-Cosel, C. Rangacharyulu, A. Richter, G. Schrieder, K. Schweda, and J. Wambach, Phys. Rev. Lett. **85** (2000) 2913.

[26] H. Diesener, U. Helm, P. von Neumann-Cosel, A. Richter, G. Schrieder, A. Stascheck, A. Stiller, and J. Carter, Nucl. Phys. **A696** (2001) 272.

[27] P. von Neumann-Cosel, A. Richter, G. Schrieder, A. Shevchenko, A. Stiller, and H. Arenhövel, Phys. Rev. Lett. **88** (2002) 202304.

[28] P. von Neumann-Cosel, F. Neumeyer, S. Nishizaki, V. Yu. Ponomarev, C. Rangacharyulu, B. Reitz, A. Richter, G. Schrieder, D. I. Sober, T. Waindzoch, and J. Wambach, Phys. Rev. Lett. **82** (1999) 1105.

[29] B. Reitz, A. M. van den Berg, D. Frekers, F. Hofmann, M. de Huu, Y. Kalmykov, H. Lenske, P. von Neumann-Cosel, V. Yu. Ponomarev, S. Rakers, A. Richter, G. Schrieder, K. Schweda, J. Wambach, and H. J. Wörtche, Phys. Lett. **B532** (2002) 179.

[30] N. Ryezayeva, *Search for the $p_{1/2^-}$ resonance in ^{7}He with the ^{7}Li(d,^{2}He) reaction and measurement of the deuteron electrodisintegration under 180° at the S-DALINAC*, Dissertation D17, TU Darmstadt (2006).

[31] H.-D. Gräf, H. Miska, E. Spamer, O. Titze, and T. Walcher, Nucl. Instr. Meth. **153** (1978) 9.

[32] T. Walcher, R. Frey, H.-D. Gräf, E. Spamer, and H. Theissen, Nucl. Instr. Meth. **153** (1978) 17.

[33] D. Schüll, J. Foh, H.-D. Gräf, H. Miska, R. Schneider, E. Spamer, H. Theissen, O. Titze, and T. Walcher, Nucl. Instr. Meth. **153** (1978) 29.

[34] J. Foh, R. Frey, R. Schneider, A. Schwierczinski, H. Theissen, and O. Titze, Nucl. Instr. Meth. **153** (1978) 43.

[35] A. W. Lenhardt, *Entwicklung eines Si-Mikrostreifendetektors für das 169°-Spektrometer am S-DALINAC*, Dissertation D17, TU Darmstadt (2004).

[36] A. W. Lenhardt, U. Bonnes, O. Burda, P. von Neumann-Cosel, M. Platz, A. Richter, and S. Watzlawik, Nucl. Instr. Meth. **A562** (2006) 320.

[37] O. Burda, *Design of a shielding for the new focal plane detector system of the energy-loss spectrometer at the S-DALINAC*, Diploma thesis, Karazin Kharkiv National University, Ukraine (2002).

[38] J. Carter, A. A. Cowley, H. Diesener, R. W. Fearick, S. V. Förtsch, M. N. Harakeh, J. J. Lawrie, S. J. Mills, P. von Neumann-Cosel, R. T. Newman, J. V. Pilcher, A. Richter, K. Schweda, F. D. Smit, G. F. Steyn, S. Strauch, and D. M. Whittal, Nucl. Phys. **A630** (1998) 631.

[39] J. Carter, A. A. Cowley, H. Diesener, R. W. Fearick, S. V. Förtsch, J. J. Lawrie, P. von Neumann-Cosel, J. V. Pilcher, A. Richter, K. Schweda, F. D. Smit, G. F. Steyn, and S. Strauch, Phys. Rev. **C63** (2001) 057602.

[40] K. Schweda, J. Carter, A. A. Cowley, H. Diesener, R. W. Fearick, S. V. Förtsch, J. J. Lawrie, P. von Neumann-Cosel, J. V. Pilcher, A. Richter, F. D. Smit, G. F. Steyn, and S. Strauch, Phys. Lett. **B506** (2001) 247.

[41] A. Shevchenko, J. Carter, R. W. Fearick, S. V. Förtsch, H. Fujita, Y. Fujita, Y. Kalmykov, D. Lacroix, J. J. Lawrie, P. von Neumann-Cosel, R. Neveling, V. Yu. Ponomarev, A. Richter, E. Sideras-Haddad, F. D. Smit, and J. Wambach, Phys. Rev. Lett. **93** (2004) 122501.

[42] S. Strauch and F. Neumeyer, *Computer program FIT*, unpublished.

[43] F. Neumeyer, *Untersuchung magnetischer Kernanregungen in* ^{48}*Ca und* ^{90}*Zr mit hochauflösender Elektronenstreuung unter 180° am S-DALINAC*, Dissertation D17, TH Darmstadt (1997).

[44] L. W. Mo and Y. S. Tsai, Rev. Mod. Phys. **41** (1969) 205.

[45] H. Fujita, *Computer program SFit*, unpublished.

[46] J. D. Holt, N. Pietralla, J. W. Holt, T. T. S. Kuo, and G. Rainovski, nucl-th/0612070.

[47] P. Lepage, nucl-th/9706029.

[48] S. K. Bogner, T. T. S. Kuo, and A. Schwenk, Phys. Rep. **386** (2003) 1.

[49] S. K. Bogner, T. T. S. Kuo, A. Schwenk, D. R. Entem, and R. Machleidt, Phys. Lett. **B576** (2003) 265.

[50] S. K. Bogner, T. T. S. Kuo, L. Corragio, A. Covello, and N. Itaco, Phys. Rev. **C65** (2002) 051301(R).

[51] R. Machleidt, Phys. Rev. **C63** (2001) 024001.

[52] B. A. Brown, A. Etchegoyen, N. S. Godwin, W. D. M. Rae, W. A. Richter, W. E. Ormand, E. K. Warburton, J. S. Winfield, L. Zhao, and C. H. Zimmerman, NSCL report number 524, and B.A. Brown, private communication.

[53] A. F. Lisetskiy, N. Pietralla, C. Fransen, R. V. Jolos, and P. von Brentano, Nucl. Phys. **A677** (2000) 100.

[54] V. G. Soloviev, *Theory of Atomic Nuclei: Quasiparticles and Phonons*, IOP Publishing, Bristol (1992).

[55] V. Yu. Ponomarev and P. von Neumann-Cosel, Phys. Rev. Lett. **82** (1999) 501.

[56] C. A. Bertulani and V. Yu. Ponomarev, Phys. Rep. **321** (1999) 139.

[57] N. Lo Iudice and Ch. Stoyanov, Phys. Rev. **C62** (2000) 047302.

[58] N. Lo Iudice and Ch. Stoyanov, Phys. Rev. **C65** (2002) 064304.

[59] A. E. L. Dieperink, F. Iachello, A. Rinat, and C. Creswell, Phys. Lett. **B76** (1978) 135.

[60] O. Scholten and H. Kruse, Phys. Lett. **B125** (1983) 113.

[61] H. Sagawa, O. Scholten, and B. A. Brown, Nucl. Phys. **A462** (1987) 1.

[62] P. Van Isacker, K. Heyde, J. Jolie, and A. Sevrin, Ann. Phys. **171** (1986) 253.

[63] J. Heisenberg and H. P. Blok, Annu. Rev. Nucl. Part. Sci. **33** (1983) 569.

[64] J. Raynal, *code DWBA05*, NEA data bank NEA-1209.

[65] M. A. Franey and W. G. Love, Phys. Rev. **C31** (1985) 488.

[66] F. Hofmann, C. Bäumer, A. M. van den Berg, D. Frekers, V. M. Hannen, M. N. Harakeh, M. A. de Huu, Y. Kalmykov, P. von Neumann-Cosel, V. Yu. Ponomarev, S. Rakers, B. Reitz, A. Richter, A. Shevchenko, K. Schweda, J. Wambach, and H. J. Wörtche, Phys. Lett. **B612** (2005) 165.

[67] R. De Leo, H. Akimune, N. Blasi, I. Daito, Y. Fujita, M. Fujiwara, S. I. Hayakawa, S. Hatori, K. Hosono, H. Ikegami, T. Inomata, I. Katayama, K. Katori, L. Lagamba, S. Micheletti, S. Morinobu, T. Nakagawa, S. Nakayama, A. Narita, T. Noro, R. Perrino, M. Pignanelli, H. Sakaguchi, J. Takamatsu, A. Tamii, K. Tamura, M. Tanaka, A. Terakawa, T. Tohei, M. Tosaki, T. Yamagata, A. Yamagoshi, M. Yosimura, and M. Yosoi, Phys. Rev. **C53** (1996) 2718.

[68] P. D. Kunz, *code CHUCK3*, unpublished.

[69] P. Schwandt, H. O. Meyer, W. W. Jacobs, A. D. Bacher, S. E. Vigdor, M. D. Kaitchuck, and T. R. Donoghue, Phys. Rev. **C26** (1982) 55.

[70] N. Lo Iudice and Ch. Stoyanov, Phys. Rev. **C73** (2006) 037305.

[71] E. Elhami, J. N. Orce, S. Mukhopadhyay, S. N. Choudry, M. Scheck, M. T. McEllistrem, and S. W. Yates, Phys. Rev. **C75** (2007) 011301(R).

[72] Steven C. Pieper and R. B. Wiringa, Annu. Rev. Nucl. Part. Sci. **51** (2001) 53.

[73] D. R. Tilley, J. H. Kelley, J. L. Godwin, D. J. Millener, J. E. Purcell, C. G. Sheua, and H. R. Weller, Nucl. Phys. **A745** (2004) 155.

[74] S. E. Woosley and R. D. Hoffman, Astrophys. J. **395** (1992) 202.

[75] B. S. Meyer, G. J. Mathews, W. M. Howard, S. E. Woosley, and R. D. Hoffman, Astrophys. J. **399** (1992) 656.

[76] W. M. Howard, S. Goriely, M. Rayet, and M. Arnould, Astrophys. J. **417** (1993) 713.

[77] S. E. Woosley, J. R. Wilson, G. J. Mathews, R. D. Hoffman, and B. S. Meyer, Astrophys. J. **433** (1994) 229.

[78] H. Utsunomiya, Y. Yonezawa, H. Akimune, T. Yamagata, M. Ohta, M. Fujishiro, H. Toyokawa, and H. Ohgaki, Phys. Rev. **C63** (2001) 018801.

[79] G. Küchler, A. Richter, and W. von Witsch, Z. Phys. **A326** (1987) 447.

[80] J. P. Glickman, W. Bertozzi, T. N. Butti, S. Dixit, F. W. Hersman, C. E. Hyde-Wright, M. V. Hynes, R. W. Lourie, and B. E. Norum, Phys. Rev. **C43** (1991) 1740.

[81] H.-G. Clerc, K. J. Wetzel, and E. Spamer, Nucl. Phys. **A120** (1968) 441.

[82] F. C. Barker, Aust. J. Phys. **53** (2000) 247.

[83] A. M. Lane and R. G. Thomas, Rev. Mod. Phys. **30** (1958) 257.

[84] G. Breit and W. Wigner, Phys. Rev. **49** (1936) 519.

[85] H. Theissen, *Spectroscopy of Light Nuclei by Low Energy (< 70 MeV) Inelastic Electron Scattering*, Springer Tracts in Mod. Phys. **65** (1972) 1.

[86] F. Ajzenberg-Selove, Nucl. Phys. **A506** (1990) 1.

[87] P. M. Endt, Nucl. Phys. **A633** (1998) 1.

[88] P. Navrátil, J. P. Vary, and B. R. Barrett, Phys. Rev. Lett. **84** (2000) 5728.

[89] P. Navrátil, J. P. Vary, and B. R. Barrett, Phys. Rev. **C62** (2000) 054311.

[90] C. Forssén, P. Navrátil, and W. E. Ormand, Phys. Rev. **C71** (2005) 044312.

[91] C. Forssén, private comunication.

[92] C. Angulo, M. Arnould, M. Rayet, P. Descouvemont, D. Baye, C. Leclercq-Willain, A. Coc, S. Barhoumi, P. Aguer, C. Rolfs, R. Kunz, J. W. Hammer, A. Mayer, T. Paradellis, S. Kossionides, C. Chronidou, K. Spyrou, S. Degl'Innocenti, G. Fiorentini, B. Ricci, S. Zavatarelli, C. Providencia, H. Wolters, J. Soares, C. Grama, J. Rahighi, A. Shotter, and M. Lamehi Rachti, Nucl. Phys. **A656** (1999) 3.

[93] J. Friedrich and N. Voegler, Phys. Lett. **B217** (1989) 220.

Danksagung

All denen, die mich durch ihren überdurchschnittlichen Einsatz bei der Entstehung dieser Arbeit unterstützt haben, möchte ich an dieser Stelle herzlich danken.

Mein besonderer Dank gilt Herrn Professor Dr. Dr. h.c. mult. A. Richter, der mir die Möglichkeit gab, an der Technischen Universität Darmstadt zu promovieren. Mit großem Interesse und Unterstützung hat er den Fortgang meiner Arbeit begleitet. Er hat es mir ermöglicht, an Schulen, Tagungen und Konferenzen teilzunehmen. Dies hat meine Sichtweite entscheidend erweitert und war eine wichtige Erfahrung für mich.

Herrn Professor Dr. N. Pietralla danke ich für die Übernahme des Korreferates.

Herr Professor Dr. P. von Neumann-Cosel hat mir in allen Phasen der Promotion mit Rat und Tat geholfen. Er war immer ein ständiger und wichtiger Ansprechpartner. Dafür möchte ich mich ganz herzlich bedanken.

I am very grateful to Dr. V. Yu. Ponomarev for providing me with QPM calculations and for his support in numerous discussions and the theoretical interpretations of the experimental results.

I would like to thank Dr. C. Forssén for providing me with NCSM calculations.

Danken möchte ich auch Herrn Dr. H.-D. Gräf für seine kompetente und geduldige Beantwortung von Fragen rund um den S-DALINAC und das 169°-Spektrometer.

Herrn Dr. H. Genz danke ich besonders für seine großartige Hilfe und Unterstützung in allen Fragen und Problemen.

Bei allen derzeitigen Mitarbeitern der Spektrometer-Gruppe und meinen früheren Kollegen, insbesondere Dr. A. W. Lenhardt, Dr. Y. Kalmykov und M. Chernykh, möchte ich mich für die Hilfe und für die gute Zusammenarbeit bedanken.

I would like to thank the collaborators from South Africa for providing the (p,p′) data, especially Dr. H. Fujita for his help with the raw data analysis.

Die vorliegende Arbeit wurde gefördert durch die DFG im Rahmen des Sonderforschungsbereichs SFB 634 und der Vorhaben NE 679/2-2, SUA-111/3/04, sowie durch die National Research Foundation, Südafrika.

Lebenslauf

Oleksiy Burda

23. März 1979	Geboren in Kharkiv, Ukraine
1986 – 1996	Besuch der Sekundärschule Nr. 59, Kharkiv, Ukraine
1996 – 2002	Studium der Physik an der Fakultät für Physik und Technik der Karazin Kharkiv National University, Ukraine. Vertiefungsrichtung - Kernphysik
1999 – 2000	Ausbildung zum Offizier
1999 – 2000	Laborassistent an der Fakultät für Physik und Technik der Karazin Kharkiv National University im Rahmen des Projektes "The elaboration of the combined telescope for measurement of high energy charge fluxes in the near Earth space and in dosimetry purposes"
Juli 2001 – Feb. 2002	Diplompraktikum am Institut für Kernphysik der Technische Universität Darmstadt
Februar 2002	Abschluss des Studiums mit Diplom mit Auszeichnung. Thema: "Design of a shielding for the new focal plane detector system of the energy-loss spectrometer at the S-DALINAC"
März – Juni 2002	Wissenschaftlicher Mitarbeiter am Institut für Kernphysik der Technische Universität Darmstadt
2002 – 2004	Stipendiat bei der FAZIT-Stiftung der Frankfurter Allgemeine Zeitung
2003 – 2006	Kollegiat des Graduiertenkollegs "Physik und Technik von Beschleunigern" an der Technische Universität Darmstadt
seit Juni 2004	Wissenschaftlicher Mitarbeiter am Institut für Kernphysik der Technische Universität Darmstadt

Erklärung:

Hiermit erkläre ich, dass ich die vorliegende Dissertation selbständig verfasst, keine anderen als die angegebenen Hilfsmittel verwendet und bisher noch keinen Promotionsversuch unternommen habe.

Darmstadt, im Juli 2007